NOAA Technical Report ERL 347-SEL 35

U.S. DEPARTMENT OF COMMERCE
NATIONAL OCEANIC AND ATMOSPHERIC ADMINISTRATION
Environmental Research Laboratories

ATS Observations of Sudden Increases of Total Electron Content Induced by EUV and X-Ray Burst of Solar Flares

R.F. DONNELLY
R.B. FRITZ

BOULDER, COLO.
SEPTEMBER 1975

U.S. DEPARTMENT OF COMMERCE
Rogers C. B. Morton, Secretary
NATIONAL OCEANIC AND ATMOSPHERIC ADMINISTRATION
Robert M. White, Administrator
ENVIRONMENTAL RESEARCH LABORATORIES
Wilmot N. Hess, Director

NOAA TECHNICAL REPORT ERL 347-SEL 35

ATS Observations of Sudden Increases of Total Electron Content Induced by EUV and X-Ray Burst of Solar Flares

R.F. DONNELLY
R.B. FRITZ

BOULDER, COLO.
September 1975

For sale by the Superintendent of Documents, U. S. Government Printing Office, Washington, D. C. 20402

TABLE OF CONTENTS

LIST OF FIGURES

LIST OF TABLES

ATS OBSERVATIONS OF SUDDEN INCREASES OF TOTAL ELECTRON CONTENT INDUCED BY EUV AND X-RAY BURST OF SOLAR FLARES

R. F. Donnelly and R. B. Fritz[1]

ATS-satellite observations of sudden increases in total electron content (SITECs) produced by extreme-ultraviolet (EUV) and X-ray bursts of solar flares are presented quantitatively and interpreted qualitatively. Large SITECs for the white-light flare of July 4, 1974, and for the large flares on July 5, September 10, and September 19, 1974, are illustrated.. The time rate of change of total electron content dN_T/dt was directly compared with SFD (Sudden Frequency Deviations) measurements. The ATS-6 dN_T/dt measurements are essentially transionospheric SFD measurements. The main difference with respect to ground-based SFD measurements is that, in addition to the 100 to 200 km altitude range where ionospheric electron loss rates are high, the ATS-6 measurements also observe the low loss-rate F2 region. Because of this low ionization loss rate, dN_T/dt includes more of the slow radiation effects and proceeds to a negative decay phase much later than the ground-based SFDs.

The Boulder ATS-6 SITECs do not exhibit a low occurrence in the morning hours reported in other studies. This may result from the higher resolution of the ATS-6 measurements and the difficulty in detecting SITECs during the morning rapid rise in total electron content. A lack of SITECs for flares near the edge of the sun is interpreted in terms of the impulsive EUV component of flare being relatively weak for flares near the solar limb because of absorption of the emission from its low lying source while propagating through the surrounding non-flaring solar atmosphere. SITECs' rapid rise, flat maximum, and decay are qualitatively interpreted in terms of the time and spectral characteristics of solar EUV and X-ray bursts and in terms of the increased F-region electron loss rates during ionospheric storms. The rapid fine structure in the EUV bursts produces corresponding fine time structure in the time rate of change of total content dN_T/dt and also in SFDs. Because the impulsive component of solar flare radiation is strong in the 100-911A range, which is important for producing O^+ and H^+ at high altitudes where electron loss rates are low, it is the major source of a SITEC and dominates the rapid rise of the SITEC and the large dN_T/dt values. The slow components of flare radiation are a significant secondary source of SITECs and are particularly important during the slow peak and decay phase of the event. The time t_N of the peak of the SITEC (ΔN_{Tmax}) always exceeds the peak time t_I of the impulsive flare component and varies from one event to another from near t_I to later than the time t_S of the peak of the slow flare component according to whether the decay time of the impulsive emission was small or large, and whether the ionosphere was stormy or quiet, respectively.

1. INTRODUCTION

X-ray and extreme ultraviolet (EUV) bursts of solar flares cause sudden ionospheric disturbances where different portions of these disturbances are observed by numerous observing techniques having a wide variety of height, intensity, and time resolution. SITECs are sudden increases in total electron content caused by solar flares and are observed by use of satellite radio transmissions through the ionosphere recorded usually with time resolution of about 1/2 min (Papagiannis and Matsoukas, 1971). Recent observations of the total columnar electron content (N_T) using the ATS-6 radio beacon experiment (Hargreaves, 1970; Davies et al., 1975) have provided sufficiently high time resolution (1 sec) and intensity resolution of SITECs to permit accurate calculation of the time rate of change of the total columnar electron content. This report presents these high-resolution ATS-6 observations of SITECs together with earlier SITEC observations by means of the ATS-1 and ATS-3 satellites.

[1]Wave Propagation Laboratory, NOAA, ERL, Boulder, Colorado 80302

Prior studies have concentrated on the maximum value of the enhancement of the total ionospheric electron content (ΔN_{Fmax}). Garriott et al. (1967) reported $\Delta N_{Fmax} \approx 2 \times 10^{16} m^{-2}$ (F denotes Faraday rotation measurements) vertically through the ionosphere for the flares of 1925 UT May 21, 1967, and 1840 UT May 23, 1967. Matsoukas et al. (1972) found that the correlation of 19 SITECs from August 1968 to August 1970 with respect to solar radio bursts at centimeter wavelengths was higher for (1) flares with large peak radio flux, (2) flares located near the center of the sun rather than near the solar limb, and (3) flares occurring near local noon or in the afternoon rather than in the early morning. In the present study, these features are discussed in terms of the properties of the X-ray and extreme ultraviolet emissions (EUV) of solar flares. Papagiannis and Matsoukas (1971) have shown a high correlation in occurrence of SITECs and large SFDs. The high resolution of the ATS-6 measurements permit detailed quantitative comparison with SFD data.

Mendillo et al. (1974) studied the global morphology of one large SITEC on August 7, 1972, using observations from 17 different ground stations, and found that the peak enhancement of Faraday total electron content ΔN_{Fmax} had the following global behavior: (1) ΔN_{Fmax} had no simple relationship to the solar zenith angle χ or to sec χ (observations included $31° \leq \chi \leq 73°$). (2) There was no simple relationship with respect to local time or longitude. (3) ΔN_{Fmax} had no simple relationship with the magnitude of geomagnetic sudden flare effects seen on nearby magnetometer recordings, but (4) ΔN_{Fmax} did increase systematically with decreasing latitude. Using incoherent scatter observations at Millstone Hill during the peak and decay stage of this SITEC, Mendillo et al. (1974) showed that only about 30% of ΔN_{Fmax} came from below 200 km and about 40% came from above 300 km.

The E- and F-region effects of solar flares have been observed by several other techniques in addition to SITECs (Mitra, 1974). Six flare events have been observed with incoherent scatter techniques (Mendillo and Evans, 1974; Thome and Wagner, 1971; Taylor, 1975). Such measurements provide moderate height resolution but low time resolution of the ionization enhancements for large solar flares where the percentage enhancement of ionization is higher than a few percent. These measurements have established that very large and long lasting percentage ionization enhancements occur in the lower E region and upper D region below the normal bottom of the E layer. Mendillo and Evans have established for the peak and decay phase of the flare event of August 7, 1972, the following important features: (1) the ionization enhancements were nearly 100% at 125 km, 60% at 200 km, with an increase in vertical total electron content of about $3.8 \times 10^{16} m^{-2}$ or about 30%, the largest F-region event observed, (2) the electron temperature increased by several hundred degrees in the F2 region, and (3) a sudden upward drift of ionization developed in the F2 region, where the drift velocity increased nearly linearly with altitude. Thome and Wagner (1971) found similar results for two large flares on May 21 and May 23, 1967, except they observed a slight decrease at high altitudes whereas an increase was observed at all altitudes for the flare of August 7, 1972. This difference may result from different preflare transport conditions for the different flares. Thome and Wagner's time resolution ($\sim$1/2 min) was sufficient to establish the following: (1) the ionization enhancement was rapid in the 100 to 200 km altitude range followed by a rapid decay of the enhancement in the 130 to 190 km altitude range, (2) the ionization enhancement in the 90 to 130 km altitude range included a slow long-lasting ionization enhancement where the largest percentage enhancements occurred and (3) above 200 km, the ionization enhancement is also long lasting, where, although the percentage enhancement is small, the absolute ionization enhancement integrated over all higher altitudes is the dominant portion of the total electron content enhancement. Because the EUV radiation of solar flares includes impulsive emissions with rise and decay times sometimes as fast as several seconds (see section 3), current incoherent scatter measurements cannot resolve the large values

of dNe/dt that occur early in solar flares. On the other hand, the few ionospheric flare events observed with incoherent scatter measurements have shown a consistent behavior in the 90 to 300 km altitude range for the slow phases of these events, including the slow-rise portion below 130 km, the peak and decay phase.

Another technique for observing E- and F-region effects of solar flares are SFDs (Sudden Frequency Deviations) measured with ground-based HF Doppler experiments wherein the received frequency of an HF radiowave reflected in the ionosphere deviates from the transmitted frequency in proportion to the time rate of change of electron density along the propagation path. Such measurements have low height resolution but high time resolution. This technique is very sensitive for detecting the ionospheric effects of impulsive solar EUV and X-ray bursts. More than 2000 events have been observed in Boulder since 1960 and several hundred SFDs have been studied in conjunction with concurrent satellite X-ray or EUV measurements. The main emphasis in our SFD studies has been to develop an understanding of the EUV and X-ray spectra and time characteristics of solar flares and the relation of these ionizing flare radiations to other solar flare phenomena (Donnelly, 1971, 1973; Donnelly and Hall, 1973; and Donnelly et al., 1973). These studies have led to models for the X-ray and EUV flare radiation, discussed qualitatively in section 7, which will be used in interpreting the SITECs discussed in the remainder of this report. SFD measurements supplement SITEC measurements by providing measurements of the E- and F1-region portion of the SITEC, particularly for the impulsive phase of the flare when dNe/dt is large. SFDs and high-resolution SITEC measurements also would supplement incoherent scatter measurements of flares by providing information on the large values of dNe/dt during the impulsive phase of flares which are not resolved by incoherent scatter measurements. The relation between SITECs and SFDs is discussed in section 6.

2. ATS TOTAL ELECTRON CONTENT MEASUREMENTS

The ATS satellites are geostationary and are therefore at 6.6 Earth radii. When the satellites were observed from Boulder they were at the locations given in Table 1. The radio beacon aboard ATS-6 transmits phase coherently at the frequencies given in Table 2. The 360-MHz transmissions provide a phase reference for the lower frequency transmissions. The 40-MHz transmissions, the first geostationary radio-beacon transmissions below 100 MHz, provide much higher resolution of N_T than previously attainable.

The Boulder ATS-6 data were searched for SITECs by examining diurnal total content curves for sudden enhancements and by using lists of Hα solar flares, microwave radio bursts and SMS-1 X-ray data to select times for further detailed examination of both the ATS-6 phase data and the time rate of change of the phase. The Boulder ATS-1 and ATS-3 measurements were examined during April and May 1973, when numerous large solar flares occurred. Figure 1 shows diurnal curves of Faraday rotation measurements. The SITECs at about 1400 UT on July 4 and at 1535 UT and 2155 UT on July 5 are distinct events where the sudden increase in total electron content is much faster than other types of variations that occur. Figure 2 shows the rise and peak of the two largest events. The largest SITEC observed (1400 UT July 4) had a peak content enhancement of only about 23% of the preflare background level. The largest SITECs are small in amplitude compared with the diurnal variation in total electron content. Some flare events in Figure 1 do not appear distinctly different from non-flare variations; however, most of these have distinct features in the high resolution time-rate-of-change of phase. The small spikes in content at 2350 UT on July 2 or at 1920 UT on July 3 were not accompanied by solar flare radiation; furthermore, the time-rate-of-change of phase for these events did not have the distinctive impulsive structure that most SITECs have. Considering the nonflare variations in Figure 1, it is clear that for most of the SITECs it is difficult to determine how much of the apparent SITEC variation is induced by the flare and how much results from other ionospheric variations.

Table 1: Total Electron Content Observations at Boulder, Colorado

Satellite	ATS-6	ATS-3	ATS-1
Satellite Location			
Latitude	0±1.8°	0±3.4°	0±5.1°
Longitude	94.0±0.5°W*	69°W	149°W
Mean 300 km Altitude Location			
Latitude	37.5°N	37.4°N	37.3°N
Longitude	104.2°W	101.5°W	110.3°W
Direction from Boulder Station			
Azimuth:	163°	132°	236°
Mean Elevation Angle:	42°	31°	26°
Boulder Observing Period			
From	June 15, 1974	1972	1970
To	June 6, 1975*	June 1974	June 1974
Transmitter Frequencies (see Table 2)		137.35MHz	137.35MHz
		Faraday Rotation Measurements Only	
Time Resolution	1 sec	5 sec**	5 sec**

*ATS-6 moved near Africa in June, 1975

** The ATS-1 and -3 data were smoothed by an R-C equivalent numerical filter with a time constant of 10 sec before being recorded. The ATS-6 data do not include such smoothing.

Table 2. ATS-6 Radio Beacon Characteristics

Carrier Frequency MHz	Modulation Frequencies MHz	Effective Radiated Power (mW)
40		500
	±0.1	250
	±1	500
140		1600
	±1	400
360		2000
	±0.1	250
	±1	250

Actual carrier and modulation frequencies are integer multiples of 100.04 KHz.

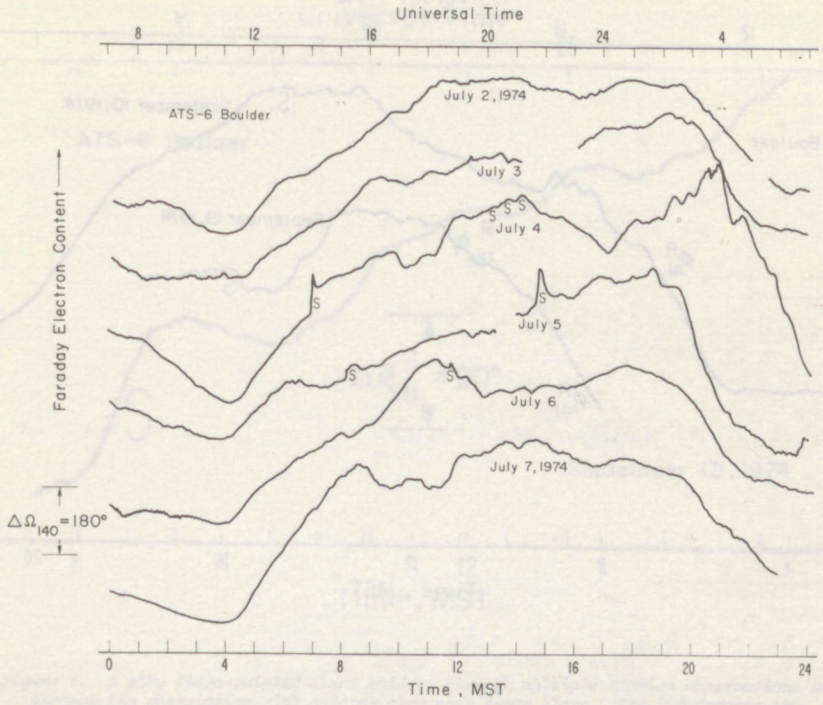

Figure 1. Diurnal Faraday-phase measurements for July 2 to 7, 1974. The "S" labels denote events related to solar flares. The rise in total content late on July 4 is related to an ionospheric storm.

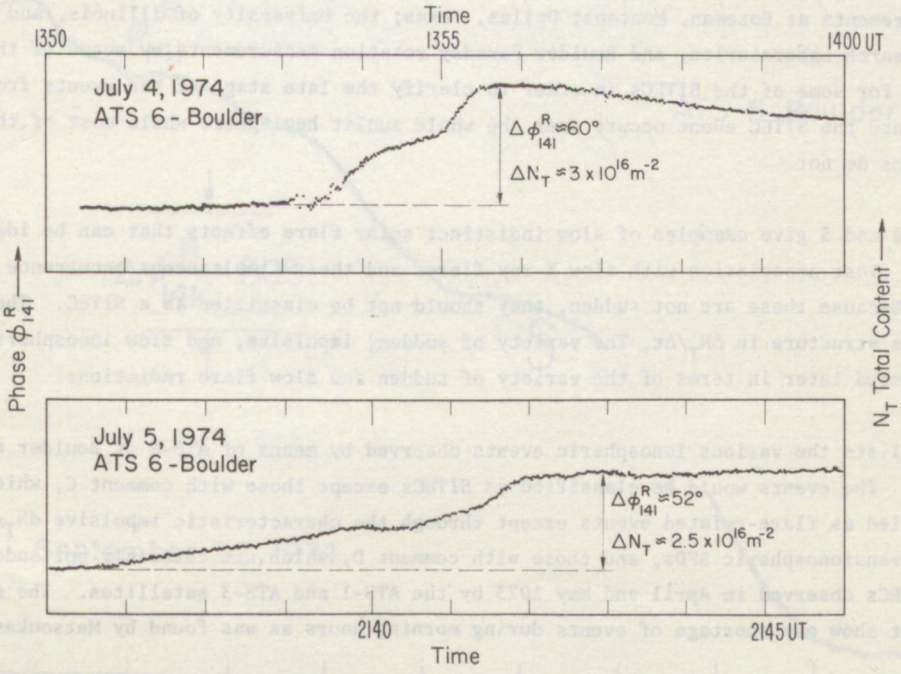

Figure 2. Large SITECs of July 4 and July 5, 1974. Note the rapid rise from start to maximum. The July 4th flare was a rare white-light flare. The total electron content enhancements refer to the slant path from ATS-6 to Boulder.

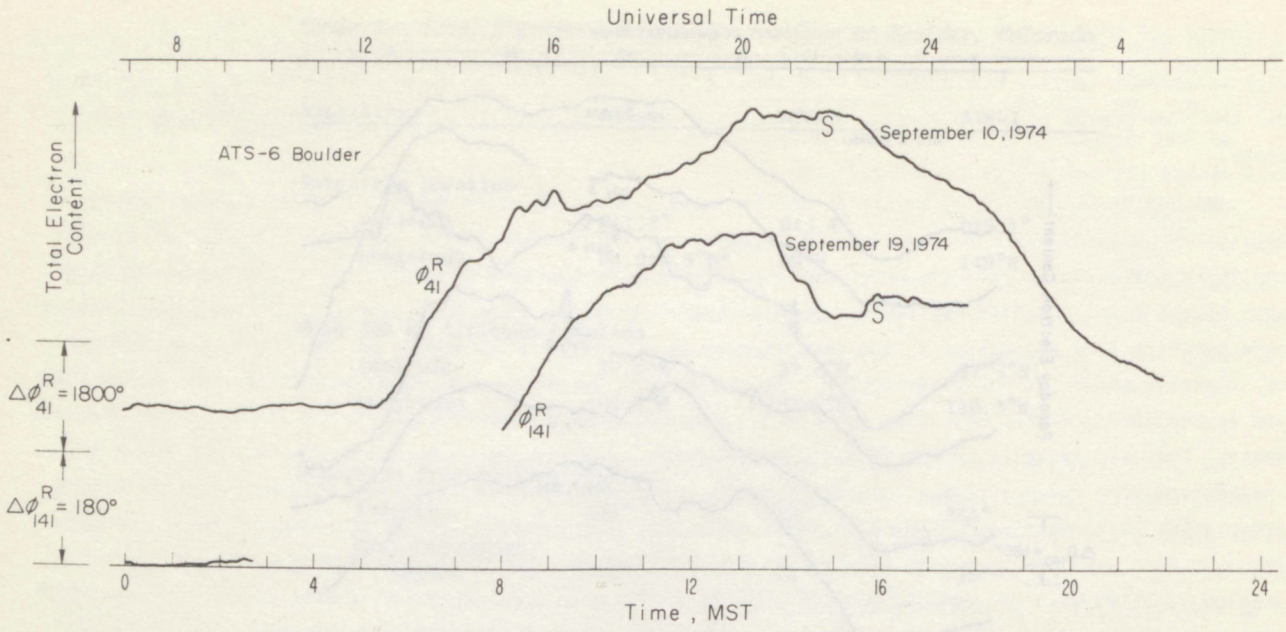

Figure 3. Diurnal total content variations and the SITECs of September 10 and 19, 1974. The "S" denotes the solar flare-related events.

Figure 3 illustrates two SITECs in September 1974 in terms of the overall daily variations. The sudden rise of these events is quite clear but the duration is much less certain. Electron columnar content measurements at Bozeman, Montana; Dallas, Texas; the University of Illinois, and the Air Force Cambridge Research Laboratories, and Boulder Faraday rotation measurements by means of the SMS-1 satellite were examined for some of the SITECs in order to clarify the late stage of the events from other ionospheric variations since the SITEC event occurs over the whole sunlit hemisphere while most of the other short term variations do not.

Figures 4 and 5 give examples of slow indistinct solar flare effects that can be identified only through their close association with slow X-ray flares and their simultaneous occurrence over the global hemisphere. Because these are not sudden, they should not be classified as a SITEC. They also lack impulsive fine structure in $\Delta N_T/\Delta t$. The variety of sudden, impulsive, and slow ionospheric flare events will be discussed later in terms of the variety of sudden and slow flare radiations.

Table 3 lists the various ionospheric events observed by means of ATS-6 at Boulder and related to solar flares. The events would be classified as SITECs except those with comment C, which are too small to be identified as flare-related events except through the characteristic impulsive dN_T/dt and are essentially transionospheric SFDs, and those with comment D, which are certainly not sudden. Table 4 lists the SITECs observed in April and May 1973 by the ATS-1 and ATS-3 satellites. The events in Tables 3 and 4 do not show any shortage of events during morning hours as was found by Matsoukas et al. (1972).

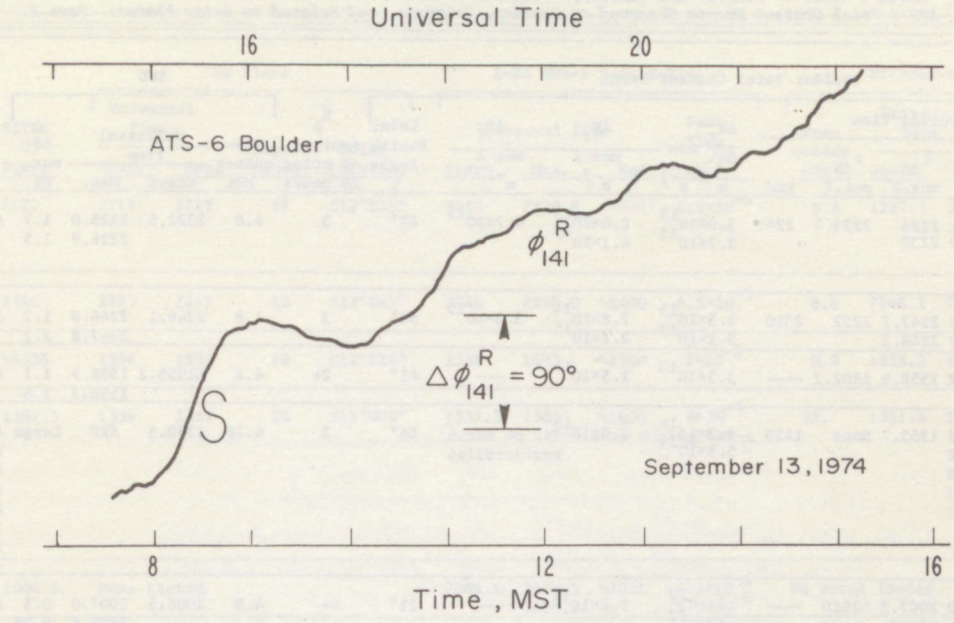

Figure 4. A slow flare-related event evident through multiple station observations and through its association with a large slow soft X-ray flare. The "S" denotes the flare-related event.

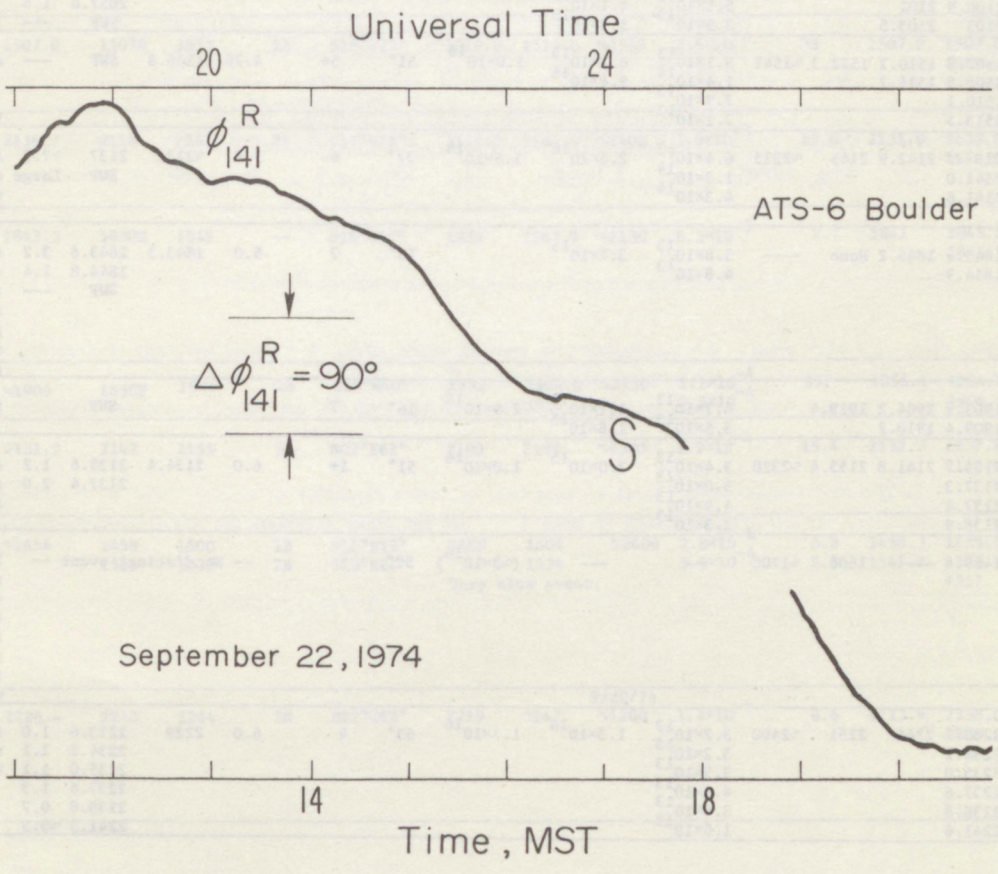

Figure 5. A slow and indistinct flare-related event.

Table 3. ATS-6 Total Content Events Observed at Boulder, Colorado, and Related to Solar Flares: Part I.

Date 1974	Boulder Total Content Event: Universal Time: UT Start	$t_{\Delta N/\Delta t}$ max	$t_{\Delta N}$ max.1	$t_{\Delta N}$ max.2	End	$\frac{\Delta N_T}{\Delta t}$ max $m^{-2}\,s^{-1}$	ΔN_T max 1 m^{-2}	ΔN_T max 2 m^{-2}	Solar Zenith Angle χ	$\bar{K}_p$ Average of prior 24 hours	SFD: Frequency MHz	SFD: Universal Time: Start	SFD: Universal Time: Max.	SFD: Δf max. Hz	Comments key on page 10
June 30	2223*	2225 2227.8	2226 2230	2233.5	2245	3.0×10^{13} 2.7×10^{13}	2.0×10^{15} 4.1×10^{15}	4.7×10^{15}	47°	3	4.8	2222.5	2225.0 2226.9	1.7 1.5	A,B,E *SITEC timing fouled by two lightning strokes.
June 30	2246*	2246.8 2247.8	2247.2 2248.2	2252	2310	2.5×10^{13} 5.1×10^{13}	7.8×10^{14} 2.1×10^{15}	3.3×10^{15}	51°	3	4.8	2246.1	2246.8 2247.8	1.2 2.2	A,B,E
July 1	∿1555	1558.3	1558.9	1602.2	----	3.5×10^{13}	1.5×10^{15}	---	41°	2+	4.8	∿1555.2	1556.9 1558.3	1.1 2.6	A,E
July 4	1352.5	1353.9 1355.1	1355.7	None	1415	4.3×10^{14} 5.5×10^{14}	3.0×10^{16}		66°	3	4.76	1350.5	SWF	Large	A, Large, White light flare, main rise in soft X-ray flare is quite fast (1353-1355 UT).
July 4	2006.5	2007.0 2008.6	2007.2 ∿2009	∿2010	----	9×10^{12} 6×10^{12}	1.6×10^{14} ---	---	21°	4-	4.8	2006.5	2007.0 2008.6	0.5 0.25	A,C,E,Very small
July 4	2016.3	2017.5	2020.2	∿2026	----	1.6×10^{13}	$\sim1.5\times10^{15}$	3×10^{15}	22°	4-	4.8	2015	2017.8	1.1	A,B,C
July 4	2030.3	2030.7 2032.4 2034.5	2033.3 2035.5	2040	∿2053	9×10^{12} 2.2×10^{13} 1.3×10^{13}	1.4×10^{15} 2.1×10^{15}	$\sim2.2\times10^{15}$	24°	4-	4.8	2030.3	2030.8 2032.3 2034.4	0.4 1.1 0.8	A,B,C
July 4	2053	2059 2100.9 2103	2059.5 2101 2103.5	2105.8	∿2148	4.8×10^{13} 5.5×10^{13} 3.5×10^{13}	3.5×10^{15} 4.1×10^{15} 5.8×10^{15}	6.3×10^{15}	30°	4-	4.8	2049.5	2050.7 2057.0 SWF	0.4 1.6 ---	A,B,E
July 5	1507.0	1507.8 1508.5 1510.1 1513.5	1510.2 1514.7	1522.3	∿1541	5.1×10^{13} 1.4×10^{14} 7.9×10^{13} 7.1×10^{13}	8.1×10^{15} 9.4×10^{15}	1.0×10^{16}	51°	5+	4.76	1506.8	SWF	---	A,B E
July 5	2136.4	2137.2 2141.0 2141.6	2142.9	2145	∿2215	6.4×10^{13} 1.9×10^{14} 4.3×10^{14}	2.6×10^{16}	2.5×10^{16}	37°	6-	5.0	∿2131	2137 SWF	>7.5 Large	A,Large,Start of soft X-ray main rise ∿2136 UT
July 6	1843.3	1843.9 1844.9	1845.2	None	----	5.8×10^{13} 4.8×10^{13}	3.7×10^{15}		16°	7	5.0	1843.3	1843.8 1844.8 SWF	3.2 2.4 ---	A,Two events close enough together they are one complex event in soft X-rays and Hα.
July 6	∿1900	1903.9 1909.4	1904.2 1910.2	1919.4		6.7×10^{13} 3.5×10^{13}	1.1×10^{15} 1.8×10^{15}	2.9×10^{15}	16°	7			SWF		E
Sept 10	2131.2	2135.7 2137.3 2137.4 2138.9	2141.8	2153.4	∿2320	3.4×10^{13} 5.0×10^{13} 4.9×10^{13} 2.3×10^{13}	7.0×10^{15}	1.0×10^{16}	51°	1+	6.0	2134.4	2135.6 2137.4	1.2 2.0	A,B,Much fine structure in $\Delta N_T/\Delta t$
Sept 13	∿1456	1459.8	-----	1605	∿1700	---	---	$(\sim3\times10^{16})$	52°	2	-- No distinct event --				B,D,very slow event, difficult to distinguish flare effect from other ionospheric variations.
Sept 19	2228.4	2233.7 2234.2 2235.0 2237.6 2238.8 2241.6	2240	2251	∿2400	3.2×10^{13} 3.2×10^{13} 3.5×10^{13} 4.4×10^{13} 3.4×10^{13} 1.6×10^{13}	1.3×10^{16}	1.7×10^{16}	63°	4	6.0	2229	2233.6 2234.2 2235.0 2237.6 2238.8 2241.5	1.0 1.1 1.1 1.3 0.7 ∿0.5	A,B,Very much fine structure.

Table 3. ATS-6 Total Content Events Observed at Boulder, Colorado, and Related to Solar Flares: Part II.

Date 1974	SITEC UT Start	Hα Flare				1-8A SMS-1 Soft X-Rays				Microwave Radio Burst			
		Universal Time		Impor-	Solar	Universal Time			Peak Flux	Fre-	Universal Time		Peak Flux
		Start	Max.	tance	Location	Start	Max.	End	Wm^{-2}	quency GHz	Start	Max.	$10^{-22} Wm^{-2} Hz^{-1}$
June 30	2223	2223	2229	SB	S12°E45°	2219	2229.8	----	6.5×10^{-5}	8.8	2217.3	2225.4 2229	503. 605.
June 30	2246	2223	2247	1B	S12°E45°	2246	2250.0	∿2400	6.5×10^{-5}	8.8	2246.1	2247.9	56.
July 1	∿1555	1556	1559	SB	S12°E24°	1536	1603	∿1700	2×10^{-5}	8.8	1555.1	1556.9 1558.3	42. 89.
July 4	1352.5	1339	1357	2B	S17°W08°	1337.5 Based on IMP-H data during SMS-1 calibrations.	1356	∿1600	8×10^{-4}	35.	1351.6	1353.6 1354.0 1354.3 1355.1 1355.5 1356.7	4150. 7081. 4450. 3770. 3190. 3946.
July 4	2006.5	None Listed				2006.4	2007.5 2010.0	∿2016	4.3×10^{-6} 5.5×10^{-6}	No event listed.			
July 4	2016.3	2014	2019	SF	S17°W13°	2016.7	2018.9	∿2030	8.0×10^{-6}	No event listed.			
July 4	2030.3	2031	(2105)	(2N)	S17°W12°	2030.3	2035.3	∿2046	1.1×10^{-5}	No event listed.			
July 4	2053	2031	2105	2N	S17°W12°	2048	2106.5	∿2300	1.2×10^{-4}	35	2053.5	2058.5	1149.
July 5	1507.0	1507E	1517	2B	S16°W23°	1510.9	1515.0	∿1715	1.9×10^{-4}	35	1507.0	1507.6 1509.7	1550. 2467.
July 5	2136.7	2118	2142	2B	S17°W26°	2119.5	2144.4	∿2400	1.0×10^{-3}	15.4	2131.0	2138.8 2142.6	2771. 2616.
July 6	1843.3	1830E	1845	--	S18°W40°	1839	1847.9	∿2130	6.3×10^{-5}	2.7	1842	1845.0 1845.5	65. 71.
July 6	∿1900	1830E	1906	2B	S18°W40°	1839	1904.0 1916	∿2130	1.2×10^{-4} 2.2×10^{-4}	35.	1856.4	1904.1 1904.8	1550. 1102.
Sept 10	2131.2	2142	2155	3N	N09°E61°	2100	2148	∿2300	1.9×10^{-4}	15.4	2132.2	2137.8 2140.0	5814. 6944.
Sept 13	∿1456	1458 1505	1500 1526	1B 2B	S12°E19° S13°E24°	1459 Very slow event.	1504 1534	∿2400	2.8×10^{-6} 5.5×10^{-4}	8.8 8.8	1458.3 1511.2	1459.4 1525.9 1557	96. 127. 65.
Sept 19	2228.4	2210	2244	2N	N12°W62°	2219	2247	9/20/74 ∿1200	1.7×10^{-4}	8.8	2223.9	2238.0 2239.6	2600. 3300.

Table 3. ATS-6 Total Content Events Observed at Boulder, Colorado, and Related to Solar Flares: Part I (Cont.).

Boulder Total Content Event											SFD				
	Universal Time											Universal Time			
Date 1974	UT Start	$t_{\Delta N/\Delta t}$ max	$t_{\Delta N}$ max.1	$t_{\Delta N}$ max.2	End	$\frac{\Delta N_T}{\Delta t}$ max $m^{-2}\ s^{-1}$	ΔN_T max 1 m^{-2}	ΔN_T max 2 m^{-2}	Solar Zenith Angle χ	$\overline{K_p}$ Average of prior 24 hours	Frequency MHz	Start	Max.	Δf max. Hz	Comments
Sept 22	2330	-----	----	0040	----	---	---	$\sim 3\times10^{16}$	$\sim 80°$	4	--	No distinct event		--	B,D,Very slow event, difficult to distinguish the flare effect from other ionospheric variations. This flare was at the west limb of the sun.
Oct. 8	1449.1	1449.4	----	----	----	1.0×10^{13}	---	---	70°	2-	4.8	1449	1449.4	0.3	A,C,E, Very small spike.
Oct. 8	1742.2	1743.1	1743.9	----	----	1.7×10^{13}	8.6×10^{14}	---	46°	2-	4.8	1742.3	1743.1	0.6	A,C,E, small.
Oct. 11	1420	1422.9 1423.5	1427	None	1430	2.2×10^{13} 2.3×10^{13}	3.8×10^{15}	---	75°	2-	4.8	1420.5	1423.0 1423.6	~ 0.6 ~ 0.7	A,C
Oct. 11	1438	1446.3 1450	1456	----	----	3.1×10^{13} 2.9×10^{13}	---	---	71°	2-	4.8	1442	1446.3	~ 0.4	Rather indistinct, during rapid morning rise of N_T.
Oct. 11	1730.8	1731.8	1732.1	None	~ 1740	---	$\sim 3\times10^{15}$	---	48°	2-	4.8	1730.3	1731.8	2.8	A,C,E,Soft X-rays decaying at 1732.
Oct. 12	1723	1729.2 1735.7	-----	----	----	5.0×10^{13} ---	---	---	48°	2	4.8	1728.2	1729.1	2.0	A,C,E
Oct. 13	2256.5	2256.9	2257.1	2301	----	1.3×10^{13}	2.7×10^{14}	$\sim 2.6\times10^{14}$	75°	6	2.4	2256.3	2256.9	0.2	A,C
Oct. 15	1324.5	1325.5	1326.1	1327.8	----	4.0×10^{13}	1.3×10^{15}	1.7×10^{15}	87°	5+	2.4	1324.5	1325.5	1.9	A,C
Nov. 5	1534	~ 1535.5	1537	~ 1550	~ 1600	---	1.4×10^{15}	---	69°	1	--	No distinct event		--	B,D, Very indistinct. GHz burst very strong at short wavelengths.

COMMENTS: A = fast rise, B = slow event, C = recognized only through $\Delta N_T/\Delta t$ data, D = recognized only through ΔN_T data and E = Noisy SITEC data relative to the size of $\Delta N_T/\Delta t$ max.

The events without comments C and D would qualify as SITECs. The ATS-6 $\Delta N_T/\Delta t$ data qualify as transionospheric SFDs for the events with comment A.

ΔN_T is the enhancement in electron content along the slant path from the ATS-6 satellite to Boulder. The ratio of slant path to vertical path at the heights of the main flare effects is about 1.5. The two types of maxima are illustrated in Figure 6 and discussed on p. 15.

Table 3. ATS-6 Total Content Events Observed at Boulder, Colorado, and Related to Solar Flares: Part II (Cont.).

Date 1974	SITEC UT Start	Hα Flare				1-8A SMS-1 Soft X-Rays				Microwave Radio Burst			
		Universal Time				Universal Time					Universal Time		
		Start	Max.	Importance	Solar Location	Start	Max.	End	Peak Flux Wm^{-2}	Frequency GHz	Start	Max.	Peak Flux $10^{-22}Wm^{-2}Hz^{-1}$
Sept 22	2330	0021E	0045D	1B	N13°W90°	2138	2400	∿1130	5×10^{-5}	9.4	2327	2340.3	2000.
Oct. 8	1449.1	1449	1456	SB	N06°E48°	1450	1454	∿1540	1×10^{-5}	15.4	1448.3	1449.3	59.
Oct. 8	1742.2	1741	1744	SN	N08°E45°	1741	1747	1800	5×10^{-6}	15.4	1742.4	1743.6	27.
Oct. 11	1420	1420	1426	1B	N10°E08°	1418	1427	>1434	2×10^{-5}	15.4	1419.8	1424.5	25.
Oct. 11	1438	1425	1441	1N	N12°W01°	1433	≤1453	∿1610	$\geq6\times10^{-5}$	15.4	1436.3	1446.3	707.
Oct. 11	1730.8	1731	1734	SB	N10°E08°	1724	1734	1755	2×10^{-5}	15.4	1731	1731.9	171.
Oct. 12	1723	1726	1732	SN	N10°W06°	1726	1736	1820	9×10^{-6}	15.4	1726.5	1729.3	82.
Oct. 13	2256.5	2251 2250	2302 2254	SN SF small	N10°W24° S17°E15°	2248	2306	∿2400	7×10^{-6}	9.4	2256	2257	195.
Oct. 15	1324.5	1323	1328	1B	N07°W47°	1323	1328	1510	5×10^{-5}	15.4	1324.2	1325	630.
Nov. 5	1534	1530	1536	1N	S12°W76°	1532	1536.4	∿1815	1.3×10^{-4}	35.	1533.4	1535.3	2481.

Table 4. Boulder April-May 1973 SITECs

Date	Time of Maximum	ATS-1				ATS-3		
	UT	Preflare N_F	Max N_F	$\frac{\Delta N_F}{N_F}$	$\frac{N_F}{\Delta t}_{max}$	Preflare N_F	N_F	$\frac{\Delta N_F}{\Delta t}$
		m^{-2}	m^{-2}		$m^{-2}s^{-1}$	m^{-2}	m^{-2}	
April 11	1406	8.5×10^{16}	$2.\times10^{15}$	2%	$4.\times10^{13}$	9.5×10^{16}	$2.\times10^{15}$	2%
April 11	1843	2.6×10^{17}	$8.\times10^{15}$	3%	1.0×10^{14}	2.2×10^{17}	$6.\times10^{15}$	3%
April 29	2100	9.4×10^{16}	1.5×10^{16}	16%	1.6×10^{14}	9.5×10^{16}	1.5×10^{16}	16%
May 5	1716	2.1×10^{17}	1.5×10^{16}	7%	1.5×10^{14}	2.0×10^{17}	1.0×10^{16}	5%
May 17	1909	1.1×10^{16}	$3.\times10^{15}$	3%	$7.\times10^{13}$	1.3×10^{17}	$3.\times10^{15}$	2%
May 18	2156	1.4×10^{17}	$3.\times10^{15}$	2%	$5.\times10^{13}$	1.4×10^{17}	$3.\times10^{15}$	2%
May 19	2245	1.2×10^{17}	1.2×10^{16}	10%	2.2×10^{14}	1.2×10^{17}	1.2×10^{16}	10%

F denotes Faraday rotation measurements. The ΔN_F values given above are converted to vertical paths from the original slant path measurements whereas all the ATS-6 results in this report are the ATS-6 to Boulder slant-path values. The maximum ΔN_F values here use the preflare N_F as a constant estimate of the nonflare background whereas the ATS-6 results use a linear extrapolation of the preflare trend.

3. CONVERSION OF ATS PHASE MEASUREMENTS TO ELECTRON TOTAL CONTENT ENHANCEMENTS

Among the various ATS-6 channels received at Boulder, the three most useful for observing SITECs are the three highest N_T resolution channels, namely ϕ_{40CP10}, Ω_{40}, and ϕ^R_{41}, in order of decreasing resolution. The carrier phase (ϕ_{40CP10}) is measured by dividing the reference carrier signal at 360 MHz down to an IF frequency (10 MHz in this case); likewise, the ionosphere measuring signal is also divided down to the same frequency and their phase difference is recorded, i.e.,

$$\phi^R_{40CP10}(t) = \frac{1}{36}\,\phi_{360R} - \frac{1}{4}\,\phi_{40R}, \qquad [1]$$

where ϕ_f is the phase at frequency f, and the R refers to the right hand circularly polarized wave or ordinary wave. Carrier phase measurements were started in August 1974 and were not available during the June and July flares in Table 3. Ω is the usual Faraday rotation.

$$\Omega_{40} = \frac{\phi_{40R} - \phi_{40L}}{2} \quad . \qquad [2]$$

The ATS-1 and ATS-3 measurements were Faraday rotation measurements at 137 MHz.

The modulation phase delay compares the modulation phase near 40 MHz ($\phi_{40R} - \phi_{41R}$) with that at the phase reference frequency, i.e.,

$$\phi^R_{41} = (\phi_{40R} - \phi_{41R}) - (\phi_{360R} - \phi_{361R}) \quad . \qquad [3]$$

In terms of the phase path P and phase refractive index μ,

$$\phi_{f\,\frac{L}{R}} = 360^\circ \frac{f}{c} P_\pm = 360^\circ \frac{f}{c} \int_A^B \mu_\pm \cos\alpha \, ds, \qquad [4]$$

where A is the ATS-6 satellite and B is the receiver in Boulder, μ is given by Appleton's formula, α is the angle between the wave normal and the ray path, and ds is the differential length along the ray path. Because of the high resolution of the Boulder ATS-6 measurements, we can compute the 1-sec differences of [1-3] to determine their time derivatives, which may be expressed as frequency deviations,

$$\Delta f_{40CP10}(t) = \frac{1}{360^\circ}\frac{d\phi_{40CP10}}{dt}; \quad \Delta f^L_{40} = \frac{1}{180^\circ}\frac{d\Omega_{40}}{dt}; \text{ and } \Delta f^R_{41} = -\frac{1}{360^\circ}\frac{d\phi^R_{41}}{dt}, \qquad [5]$$

where the signs are chosen so that increasing N_T produces positive frequency deviations. According to Bennett (1967), for fixed location transmitter (A) and receiver (B),

$$\Delta f_{f\,\frac{L}{R}} = \frac{1}{360^\circ}\frac{d\phi}{dt}\,f\,\frac{L}{R} = -\frac{f}{c}\int_A^B \frac{\partial \mu_\pm}{\partial t}\cos\alpha \, ds, \qquad [6]$$

where the partial differentials are used to denote that time varying ray path is being held constant at its instantaneous value at time t in evaluating $\partial\mu/\partial t$. In general,

$$\frac{\partial \mu}{\partial t} = \frac{1}{2\mu}\left[\frac{\partial \mu^2}{\partial N_e}\frac{\partial N_e}{\partial t} + \frac{\partial \mu^2}{\partial B_i}\frac{\partial B_i}{\partial t}\quad i = 1,2,3 \quad + \frac{\partial \mu^2}{\partial \nu}\frac{\partial \nu}{\partial t}\right] \qquad [7]$$

where N_E is the electron density, B_i are the magnetic field components, and ν is the collision frequency. The first term dominates during SITECs since flares produce large rapid ionization enhancements and because μ^2 is directly dependent on N_e but only weakly dependent on B_i or ν. The last term is negligible

since, at 40 MHz and above, $\nu/2\pi f \ll 1$ above 60 km. Although collisions are important for the amplitude of the received wave, they have a very weak effect on the phase or μ. Furthermore, at the low altitudes where collisions have their largest effects ($\partial\mu/\partial\nu$ largest), the high density neutral gas would not be affected significantly by the flare nor would the electron temperature deviate significantly from the neutral temperature; hence $\partial\nu/\partial t \simeq 0$. The second term is also very small, particularly for the carrier and modulation phase data, but it may be of minor importance for the Faraday rotation data where the magnetic field enters as a first order term. For given N_e and dN_e/dt as a function of height, latitude and longitude, equations [1 - 6] are being numerically evaluated by use of a ray tracing computer program by Jones (1966; Jones and Stephenson, 1975) with a spherical harmonic model for the Earth's magnetic field for epoch 1974 (Cain and Sweeney, 1970). The assumptions involved are that collisions and the magnetic field time variations are negligible, and that the ionosphere varies sufficiently slowly, both spatially and temporally, for ray theory to apply, i.e., slowly over distances small relative to a wave length (<8m) or slowly over times small relative to the time of flight through the main portion of the ionosphere (<0.01s). Boulder preflare ionograms are being used to estimate the bottomside ionosphere, and an 0+ height exponential decay is being used for the near topside together with an H+ scale height at higher altitudes. All effects due to refraction are thereby included. These detailed quantitative results will be presented in later papers.

For the present report, in order to provide physical insight into the ATS-6 observations and to provide good estimates of the electron content enhancements, equations [1-6] were simplified by use of the collisionless quasi-longitudinal approximation for μ, i.e.,

$$\mu^2 \approx 1 - \frac{kN_e}{f(f \pm f_L)} \quad , \qquad [8]$$

and $\cos\alpha \approx 1$, where f_L is the gyrofrequency for the component of the magnetic field along the path. Equations [1-3, 5] become (Davies et al., 1975; Garriott et al., 1970):

$$N_T = \int_A^B N_e \, ds \approx + K^R_{40CP10} \, \phi^R_{40CP10}, \qquad \frac{dN_t}{dt} \approx + K^{R'}_{40CP10} \, \frac{d\phi^R_{40CP10}}{dt}, \qquad [9]$$

$$N_T = -K^R_{41} \, \phi^R_{41} \, , \qquad \frac{dN_T}{dt} \approx -K^{R'}_{41} \, \frac{d\phi^R_{41}}{dt} \, , \qquad [10]$$

$$\overline{f}_L N_T = \int_A^B f_L \, N_e \, ds = +K_{40} \, \Omega_{40}, \qquad \text{and } \overline{f}_L \, \frac{dN_T}{dt} = +K'_{40} \, \frac{d\Omega_{40}}{dt} \, , \qquad [11]$$

where N_T is the slant-path total electron content,

$$K^{R'}_{40CP10} = \frac{2c}{360^\circ} \times \frac{10^5}{k} \left[\frac{1}{40(40+\overline{f}_L)} - \frac{1}{360(360+\overline{f}_L)} \right]^{-1} \approx 3.46\times10^{12} \, m^{-2} \, degree^{-1} \, , \qquad [12]$$

$$K^{R'}_{41} = \frac{2c}{360^\circ} \times \frac{10^6}{k} \left[\frac{1}{40+\overline{f}_L} - \frac{1}{41+\overline{f}_L} - \frac{1}{360+\overline{f}_L} + \frac{1}{361+\overline{f}_L} \right]^{-1} \approx 3.7\times10^{13} \, m^{-2} \, degree^{-1} \, , \qquad [13]$$

$$K'_{40} = \frac{2c}{360^\circ} \times \frac{10^{12}}{k} \left(40^2 - \overline{f_L^2}\right) \approx 3.3\times10^{19} \, m^{-2} \, degree^{-1} \, Hz, \qquad [14]$$

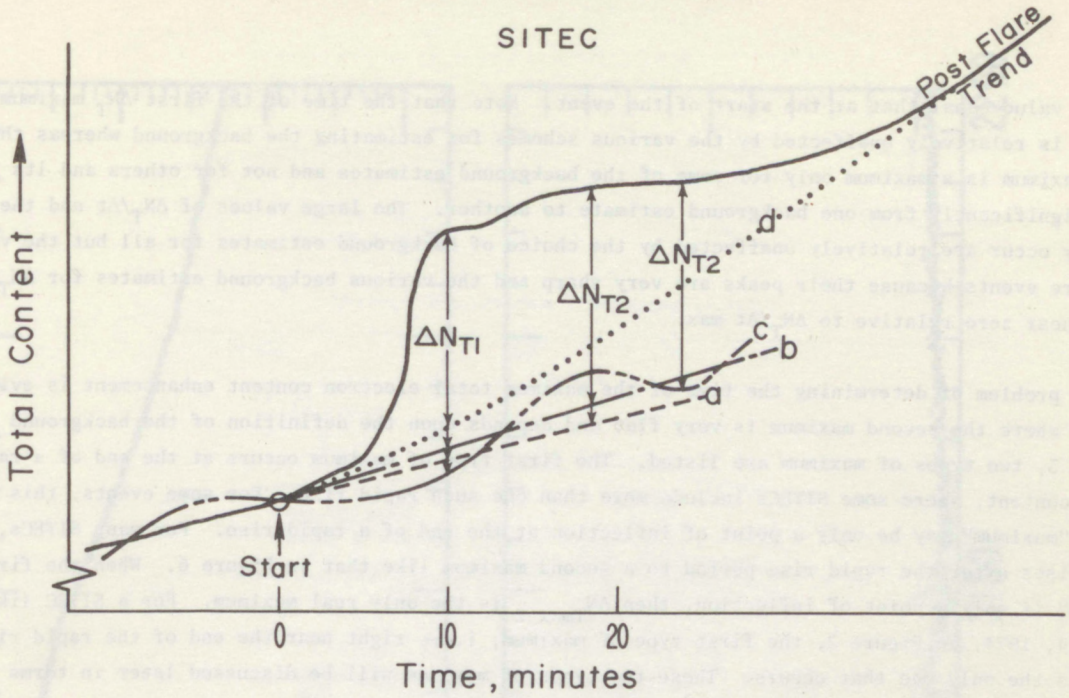

Figure 6. Problems with defining the nonflare background and the time and magnitude of the maximum enhancement in total electron content.

and $\overline{f}_L$ and $\overline{f_L^2}$ are average values of the longitudinal gyrofrequency so these terms could be removed from the ray-path integrals. The primes in K and $\overline{f}_L$ denote that the values are slightly different when dN_e/dt is the weighting factor as a function of height than when $N_e(h)$ is used, i.e., K varies slightly with time during solar flares. Equations 9-11 were used to convert the ATS-6 phase observations to the total slant-path electron content given in Table 3 (at the heights of peak electron density, the slant-path to vertical height ratio is $ds/dh \approx 1.5$). Although $\overline{f}_L$ varies with the shape of the $N_e(h)$ profile, the K factors vary by less than one percent for a wide range of realistic profile shapes (Davies et al., 1976).

Because the flare-induced enhancements of total electron content are usually small compared with other variations, e.g., diurnal, storm, and atmospheric waves, it is difficult to estimate accurately the non-flare background or to determine accurately the magnitude or the time of the maximum of the flare-induced total content enhancement. Figure 6 illustrates this problem and four approaches toward estimating the non-flare background. Curve (a), which is a linear extrapolation of the preflare trend, is the approach used for the ATS-6 results in Table 3. For some events it is difficult to distinguish the small slow beginning of the event from nonflare variations. SMS-1 soft X-ray and microwave burst data were used to help distinguish the start of the flare event. The linear extrapolation of the preflare trend should be quite good for the start, rapid rise, and early peak of the event but will usually be an increasingly poor background estimate with increasing time in the late peak and decay stage of the event. Curve (b) is the monthly median curve fitted to the start of the SITEC. This scheme did not work too well in that the day of the flare usually behaved enough differently than the monthly median that a good fit to the preflare trend was not achieved. Curve (c) represents the diurnal time curve of a day nearby that of the flare that was most similar to that of the day of the flare. Unfortunately, the total content as a function of time differs significantly from one day to another so that usually a good fit to the preflare trend was not achieved. Curve (d) involves an interpolation between the preflare and post flare trends. However, for most SITECs the end of the event is quite nebulous. Furthermore, the post flare period usually appears to be influenced by variations from atmospheric waves and other phenomena. Some prior studies apparently have measured the peak content with respect to the preflare content and therefore have in effect defined the nonflare background as if it suddenly switched to the

constant value equal that at the start of the event. Note that the time of the first ΔN_T maximum in Figure 6 is relatively unaffected by the various schemes for estimating the background whereas the second maximum is a maximum only for some of the background estimates and not for others and its time varies significantly from one background estimate to another. The large values of $\Delta N_T/\Delta t$ and the times when they occur are relatively unaffected by the choice of background estimates for all but the very slow flare events because their peaks are very sharp and the various background estimates for $\Delta N_T/\Delta t$ are all near zero relative to $\Delta N_T/\Delta t$ max.

The problem of determining the time of the maximum total electron content enhancement is evident in Figure 6 where the second maximum is very flat and depends upon the definition of the background level. In Table 3, two types of maximum are listed. The first type of maximum occurs at the end of a rapid rise in content, where some SITECs include more than one such rapid rise. For some events, this first type of "maximum" may be only a point of inflection at the end of a rapid rise. For many SITECs, ΔN_T slowly rises after the rapid rise period to a second maximum like that in Figure 6. When the first "maximum" is only a point of inflection, then $\Delta N_{T\max 2}$ is the only real maximum. For a SITEC like that of July 4, 1974, in Figure 2, the first type of maximum, i.e., right near the end of the rapid rise phase, is the only one that occurs. These two types of maximum will be discussed later in terms of their relation to the fast and slow X-ray and EUV radiations of solar flares.

4. EXAMPLES OF SITECS

Figure 7 shows the large SITEC of July 5, 1974, observed by Faraday rotation measurements at 40 MHz ($\Delta N_T = K_{40} F^{-1} \Delta\Omega_{40}$), where a slow diurnal increase occurred until 2136.6 UT, followed by a rapid rise during the impulsive flare emissions of the solar flare (2137 - 2144 UT) during the peak of the slow flare emissions, and finally a slow decay. Most of the ΔN_T enhancement occurred during the impulsive rise. The Ω curve in Figure 7 actually consists of points plotted every second which are so close together they appear to be a continuous curve except during the very rapid rise at 2141.7 UT. Because of the high time and phase resolution, we can accurately determine Δf_{40LR} (or dN_T/dt) shown in the bottom half of Figure 7, from the point to point differences in Ω_{40}. The solar flare that produced this SITEC was very intense as shown in Table 3. The soft X-ray burst was so large that the SFD data were lost owing to the high flare-induced ionospheric absorption enhancement in the D region. This SITEC was comparable in size with the May 1967 events discussed by Garriott et al. (1967) and comparable with but slightly smaller than the August 7, 1972, SITEC discussed by Mendillo et al. (1974), and the July 4 SITEC shown in Figure 2.

Figure 8 shows two small successive SITECs on June 30, 1974. The first event is just ending when the second one starts. The so-called type 1 "maximums" are actually points of inflection for these events. Figure 9 shows a medium-sized SITEC and the corresponding time rate of change in total content, which is essentially a transionospheric SFD, as will be discussed in Section 5. Figure 10 shows a small fast SITEC which occurred during an ionospheric storm. Although the diurnal variation normally increases or remains fairly constant near local noon, Figure 1 shows that on July 6, the content decreased until about 1832 UT. Despite the SITECs at 1845 and 1910 UT, the general trend was a decrease in content until 2000 UT. The rate of decrease in electron content after 1846 UT is comparable with that from 1820 to 1830 UT and from 1920 to 1955 UT. Note in Table 3 that the soft X-ray flux increased during this period until 1916 UT. It appears that ionospheric effects unrelated to the solar flare X-ray and EUV bursts were causing a general decrease in total content. All estimates for the nonflare background for this event are questionable.

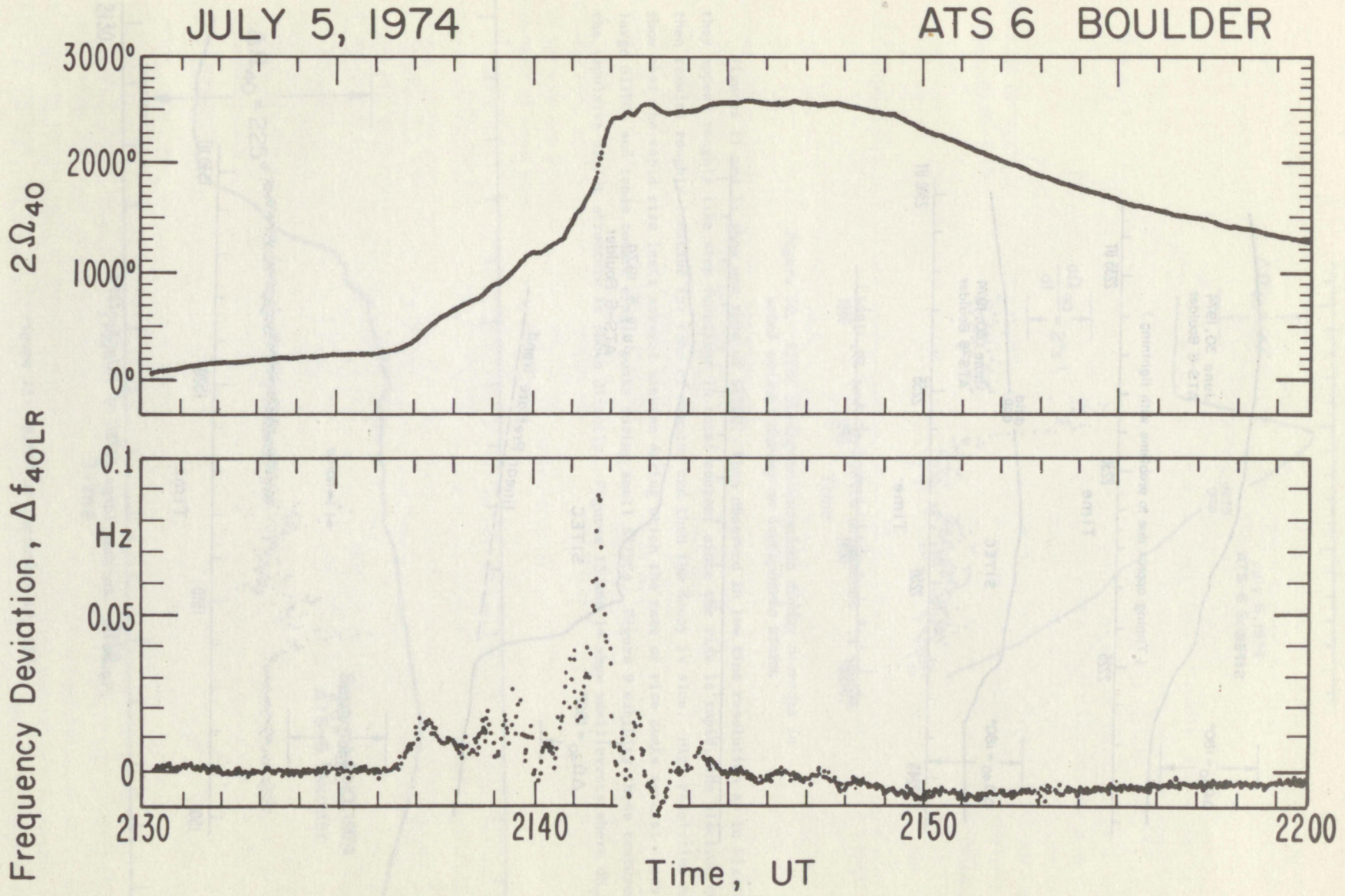

Figure 7. Large SITEC of July 5, 1974. An ionospheric storm is in progress. Preflare noise in f_{40LR} ± 0,001 Hz. The dN_T/dt points are plotted every 2 sec in this example.

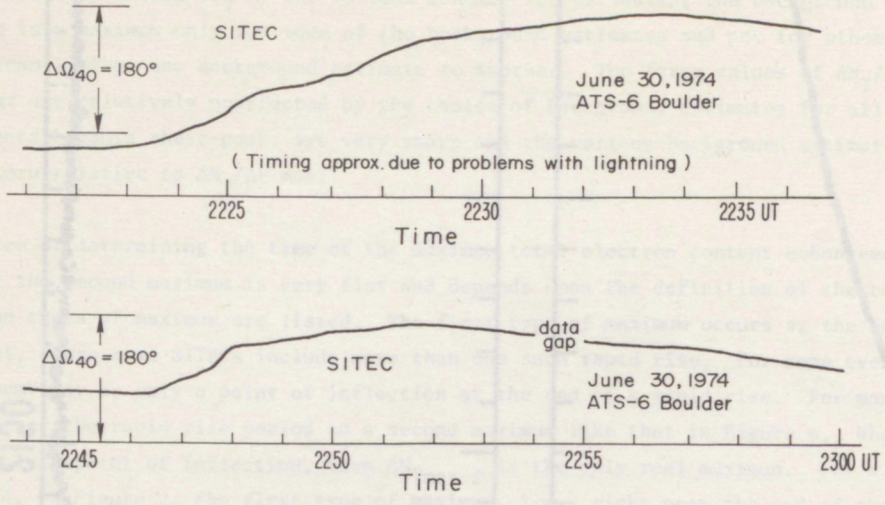

Figure 8. Successive SITECs of June 30, 1974.

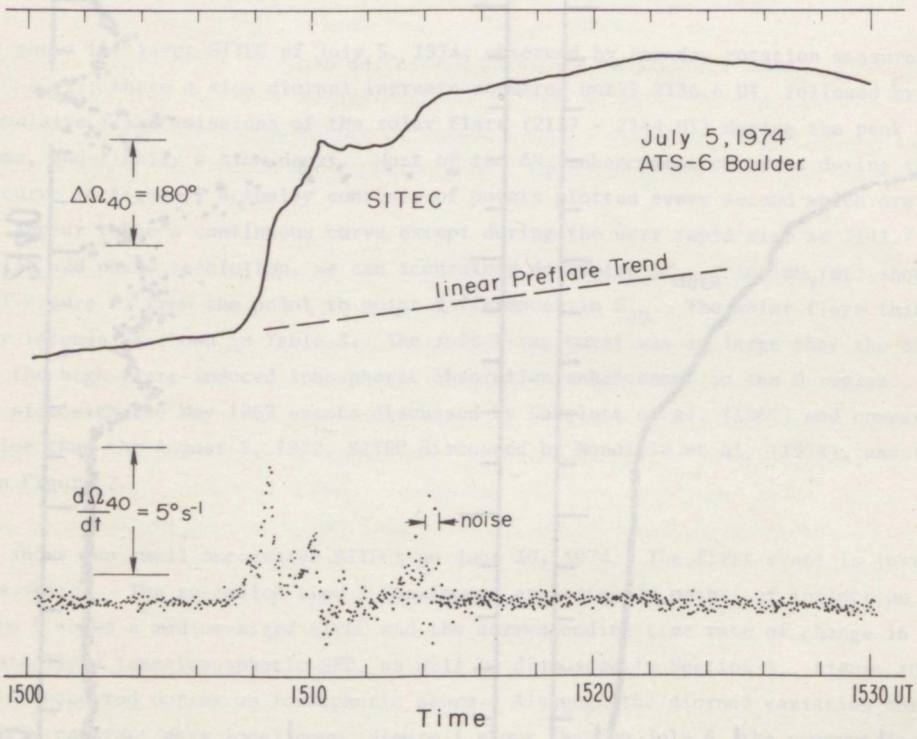

Figure 9. Another large SITEC of July 5, 1974.

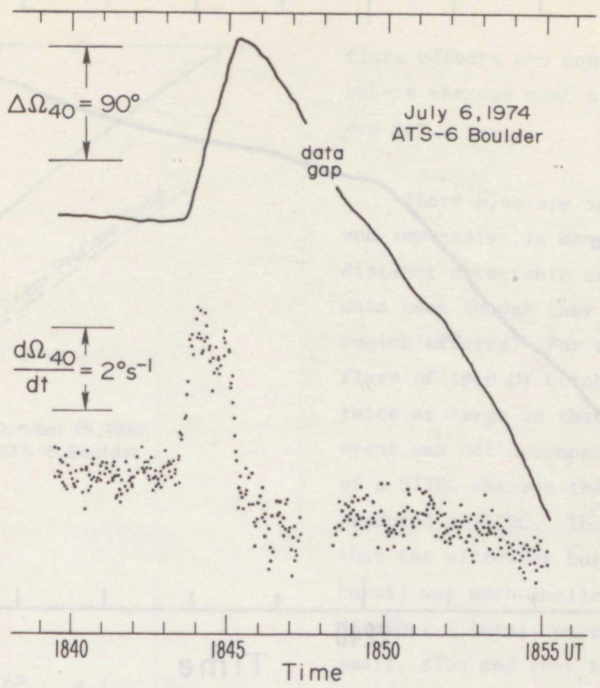

Figure 10. SITEC during an anomalous midday decrease in total content during an ionospheric storm.

Figures 11 and 12 show one type of SITEC. When observed in low time resolution as in Figure 3, they appear roughly like step functions in total content since the rise is rapid, the electron content then remains roughly constant for tens of minutes and then the decay is slow. High resolution measurements show that the rapid rise lasts several minutes during which the rate of rise peaks several times for large SITECs and tends toward single peaks during small SITECs. Figure 9 exhibits these features where the impulsive dN_T/dt structure is shown directly. Figures 13 and 14 show small events where dN_T/dt is a

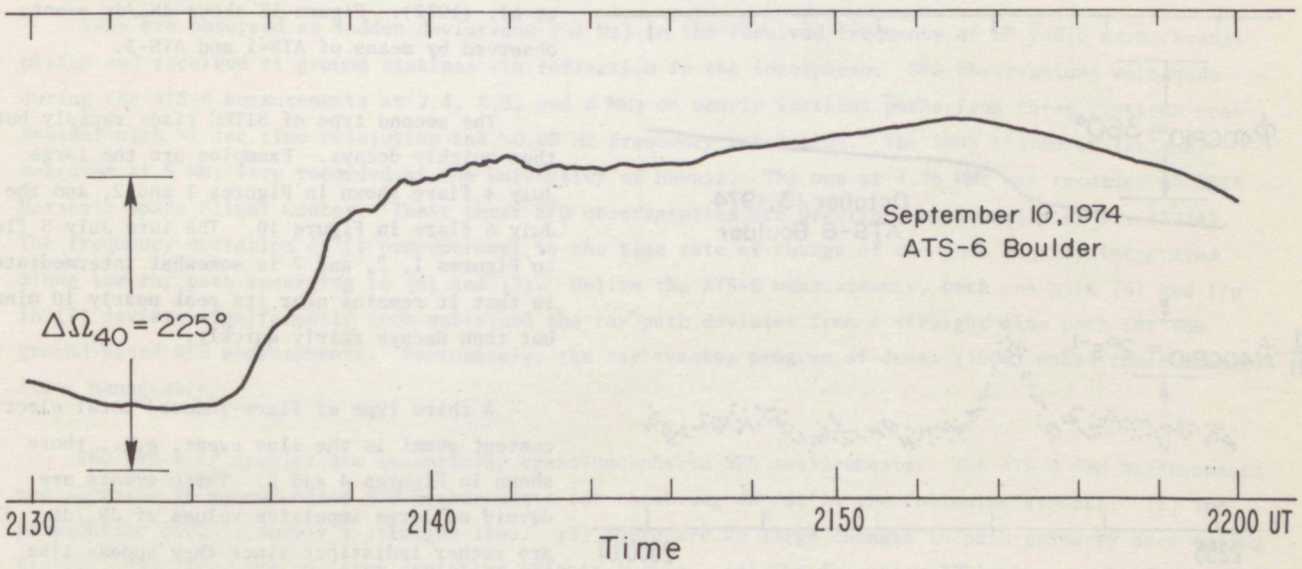

Figure 11. SITEC of September 10, 1974.

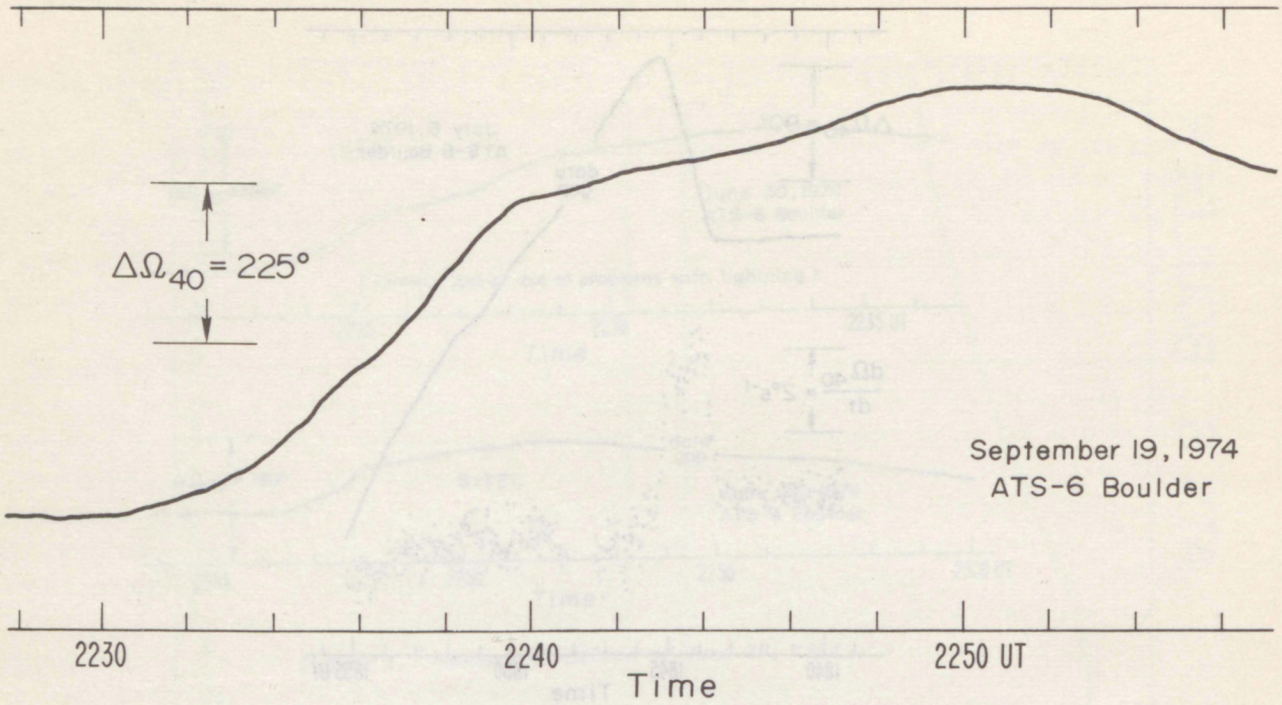

Figure 12. SITEC of September 19, 1974.

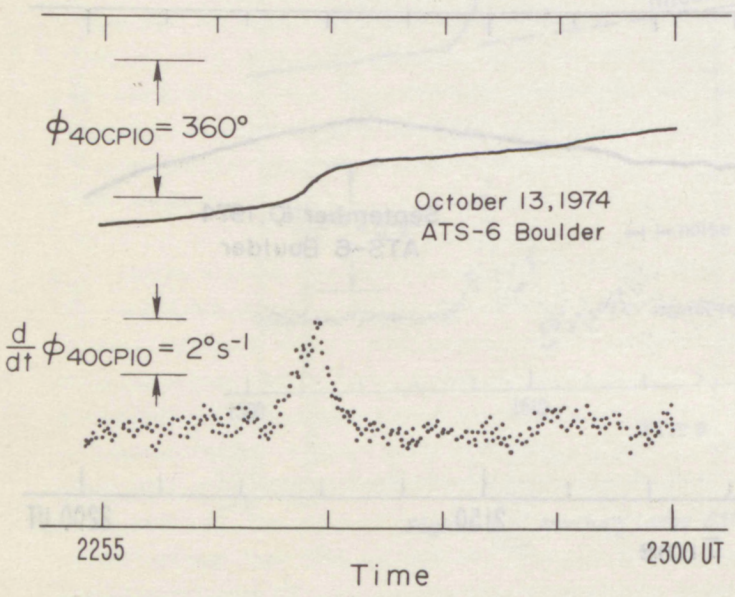

Figure 13. Small step-function and simple spike SFD of October 13, 1974.

simple spike. The event of Figure 14 occurred during early morning when the content was steadily increasing so that the linear extrapolation of the preflare data is a good estimate of the nonflare background. Low resolution observations would not detect this as a distinct event; perhaps the difficulty in distinguishing SITECs during the morning rapid rise caused the shortage of SITECs during morning hours found by Matsoukas et al. (1972). Figure 15 shows dN_T/dt events observed by means of ATS-1 and ATS-3.

The second type of SITEC rises rapidly but then quickly decays. Examples are the large July 4 flare shown in Figures 1 and 2, and the July 6 flare in Figure 10. The late July 5 flare in Figures 1, 2, and 7 is somewhat intermediate in that it remains near its peak nearly 10 minutes but then decays fairly quickly.

A third type of flare-induced total electron content event is the slow event, e.g., those shown in Figures 4 and 5. These events are devoid of large impulsive values of dN_T/dt. They are rather indistinct since they appear like other variations in total content unrelated to solar X-ray and EUV bursts. However, the solar

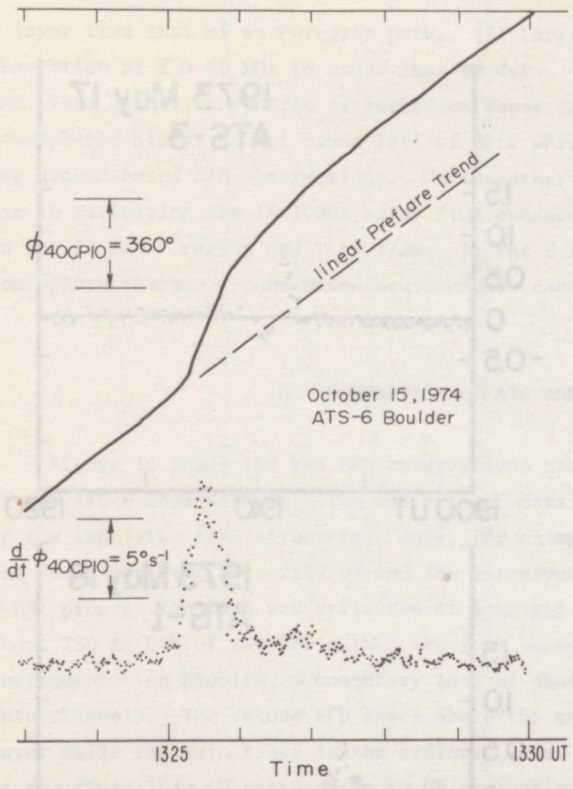

Figure 14. Step-like SITEC and simple spike SFD during the early morning rapid rise in total content.

flare effects are concurrent in the sunlit hemisphere whereas most other ionospheric variations are not.

There also are solar flares that are large and impressive in many respects that produced no distinct detectable effects in the total content data even though they produce large D- and E-region effects. For example, the 1-8A soft X-ray flare of 1910 UT October 12, 1974, was more than twice as large as that at 1722 UT, yet the later event was not accompanied by any distinct evidence of a SITEC whereas the early event definitely produced a SITEC. The clue to this puzzle is that the microwave burst (and hence the EUV burst) was much smaller for the later flare. The November 5 total-content event in Table 3 is small, slow and very indistinct and is not accompanied by an SFD despite the fact that the flare included a large soft X-ray burst and 35 GHz radio burst comparable to that of the large SITEC of September 19, 1974. The clue to why the 100-911A emission was weak and slow is the weakness of the radio burst below 10 GHz and the large solar central meridian distance of the flare. These differences in the flare X-ray and EUV spectra will be discussed in Section 7.

5. SFD OBSERVATIONS

SFDs are observed as sudden deviations ($\sim$1 Hz) in the received frequency of HF radio waves transmitted and received at ground stations via reflection in the ionosphere. SFD observations were made during the ATS-6 measurements at 2.4, 4.8, and 6 MHz on nearly vertical paths from three stations near Boulder with $\sim$1 sec time resolution and $\sim$0.05 Hz frequency resolution. The SFDs listed in Table 3 measured at 5 MHz were recorded at the University of Hawaii. The one at 4.76 MHz was recorded at NASA Marshall Space Flight Center. These three SFD observatories are described by Donnelly et al. (1974). The frequency deviation Δf is proportional to the time rate of change of electron density integrated along the ray path according to (6) and (7). Unlike the ATS-6 measurements, both cos α in (6) and $1/\mu$ in (7) deviate significantly from unity and the ray path deviates from a straight line path for the ground-based SFD measurements. Fortunately, the ray tracing program of Jones (1966) makes these complexities manageable.

The ATS-6 Δf results are essentially transionospheric SFD measurements. The ATS-6 SFD measurements are superior to ground-based SFD measurements for observing dN_e/dt in the following aspects: (1) The propagation path is nearly a straight line. (2) There are no large changes in path geometry even during flares. (3) There are no large deviative effects ($\mu \approx 1$). (4) The frequency deviation can be determined without requiring spectral analysis, which is required in ground-based measurements to separate the Δf results for different propagation paths, e.g., separations of Δf of a path reflected from a sporadic

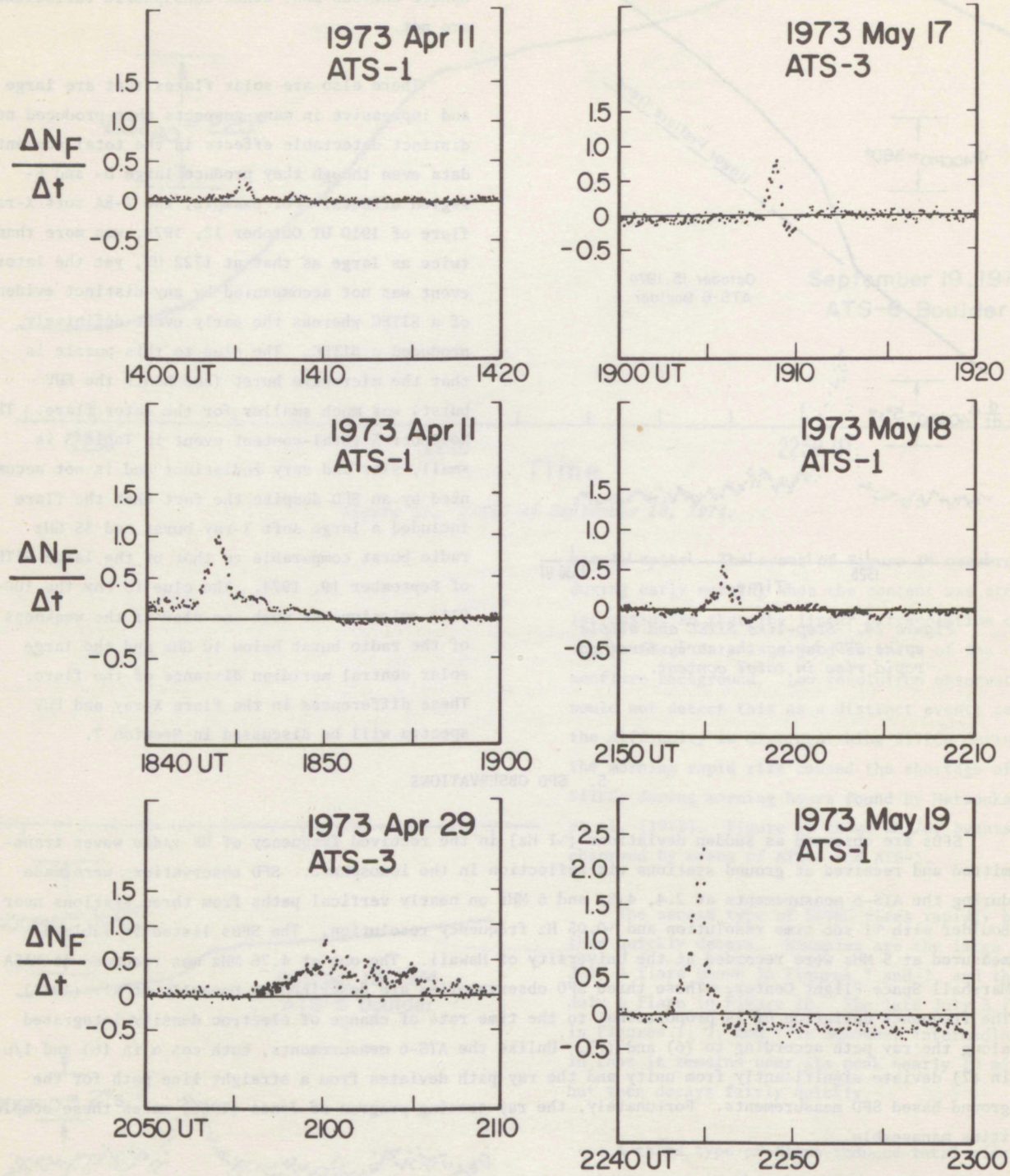

Figure 15. Transionospheric SFDs observed by means of ATS-1 and ATS-3. Units of $\Delta N_F/\Delta t$ are 10^{14} electrons $m^{-2}s^{-1}$.

E layer from that of an F-region path. (5) Large SWFs (Short Wave Fadeouts) do not cause sufficient absorption at $f \geq 40$ MHz to cause loss of data. (6) Traveling ionospheric disturbances, gravity waves, and other local ionospheric disturbances cause less "noise" relative to the flare effect. (7) Large ionospheric storms do not cause loss of data whereas low foF2 values can cause path failure (penetration) for ground-based SFD observations. On the other hand, the ATS-6 SFD measurements are more difficult to use in estimating the 10-1030A solar flux enhancement in that the electron loss time constant ($\tau \approx \beta^{-1}$ in sec in the F region and $\tau \approx 1/2\alpha N_e$ in the E region) varies greatly with altitude through the entire ionosphere whereas ground-based measurements can limit the height range to where τ is roughly constant.

6. COMPARISON OF ATS AND GROUND-BASED SFD OBSERVATIONS

Figure 16 shows the raw SFD observations near Boulder in comparison with the time-rate-of-change of the ATS-6 observations. The two sets of data agree closely in time of occurrence and relative intensity of the impulsive fine structure. Note, for example, the four small peaks in the 6-MHz SFD data along the rise from 2138.3 to 2139 UT and the corresponding concurrent small peaks in the ATS-6 data. The 6-MHz propagation path was reflected at a height of about 226 km. The ATS-6 path at that height is about 250 km SSE of the SFD path. The four anomalous ATS-6 points near 2141.2 UT are caused by an instrumentation problem, a momentary loss of phase lock which did not occur on some of the other ATS-6 data channels. The second SFD trace above the main trace near 2135.5 UT is because of the extraordinary wave, while the main trace is the ordinary wave. The extraordinary wave fades out near 2135.7 UT because of the flare-induced enhancement in HF absorption (SWF). The main SFD trace likewise becomes quite faint after 2140 UT. The SFD observations at 4.8 MHz (height of reflection $\sim$186 km) show similar agreement for the impulsive fine structure. The 18 events in Table 3 observed from ATS-6 at Boulder for which SFD observations were measured on paths reflected in the F region showed the impulsive fine structure was concurrent in the ATS-6 Δf results and SFD measurements to within our experimental accuracies. The ATS-1 and ATS-3 results differed from the ground-based SFDs slightly in timing and impulsiveness in accordance with the smoothing from the 10-sec numerical filter in the ATS-1 and ATS-3 recording system.

There are systematic differences in the slow time structure between the ground-based SFD and ATS-6 observations. Figure 17 illustrates some of the observed differences, where the impulsive fine structure is concurrent like that in Figure 16, but the slow rise from 2229 to 2237 UT is much weaker relative to the impulsive structure in the ground-based SFD observations than in the ATS-6 measurements. The ground-based SFDs start their main negative decay phase ($\Delta f < 0$, $\partial N_e/\partial t < 0$) earlier than the ATS-6 observations. For example, for the event in Figure 17, the start of the negative decay phase of the 6 MHz SFD is at about 2239.5 UT whereas the ATS-6 observations drop to small positive values but remain above zero until about 2250 UT and then proceed to a main negative decay phase, i.e., the time when the height-integrated electron density starts to decrease is more than 10 minutes later for the ATS-6 measurements than for the 6-MHz data. Small slow rises in Δf_{40CP10} were observed at the start of some solar flares before the start of Δf in ground-based SFD observations. These differences are more pronounced the lower the height of reflection of the SFD (excluding E-layer reflection heights), which is evident from comparing the 4.8- and 6-MHz SFD data, and depend on whether the ionosphere is quiet or stormy. For example, the September 10 flare in Figure 16 occurred during a geomagnetic quiet period while the flares in Figures 7, 9, 10, and 17 occurred during disturbed periods.

7. SOLAR X-RAY AND EUV BURSTS

The spectra of solar flare radiation always varies during a flare and varies appreciably from one flare to another. However, there are certain common physical patterns to the X-ray and EUV emissions

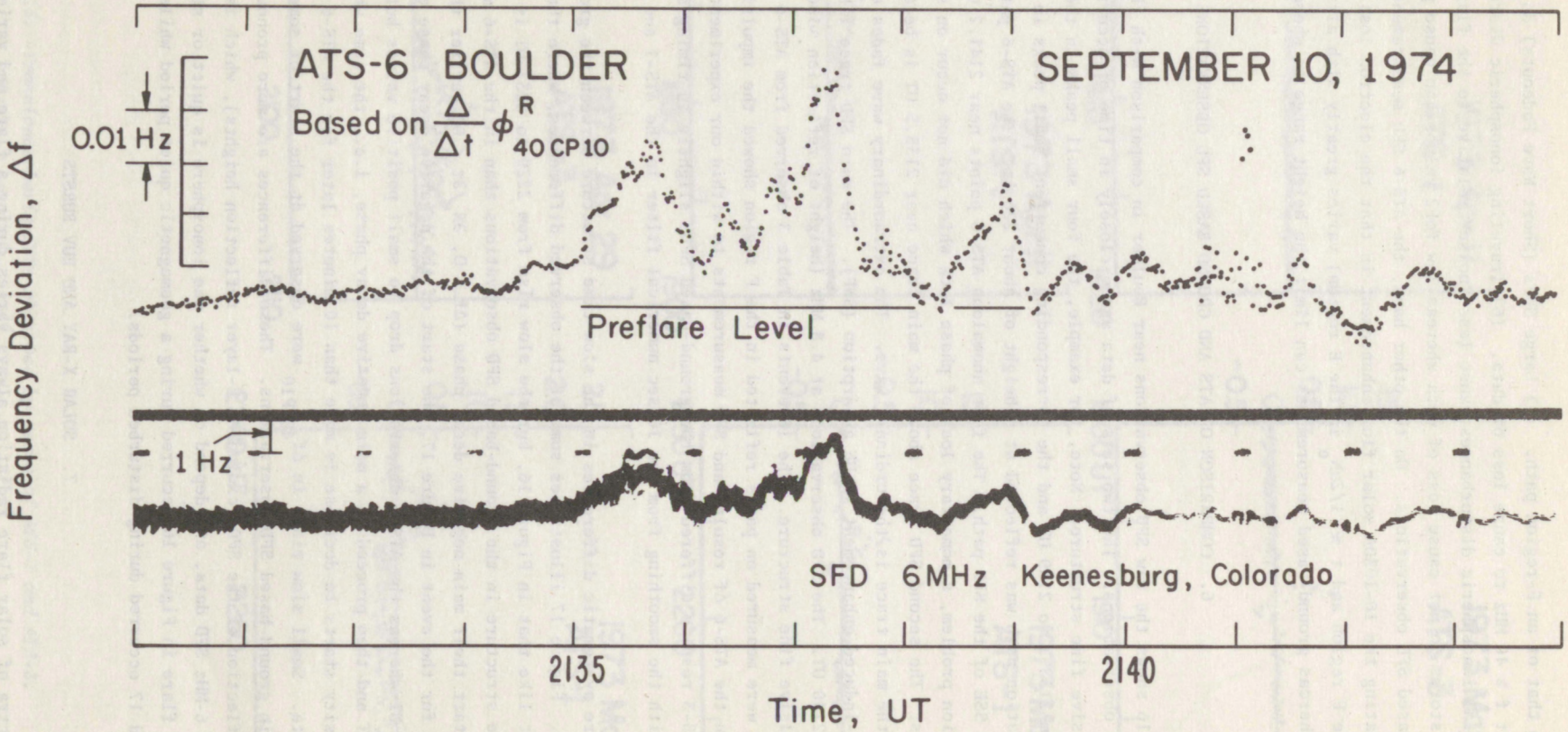

Figure 16. Concurrent ground-based and ATS-6 transionospheric SFD observations.
Δf_{max} *= 2 Hz on 6 MHz and 0.043 Hz for 40 cp 10. Preflare noise*
$\Delta f_{max} \simeq \pm 0.001$ *Hz for 40 cp 10.*

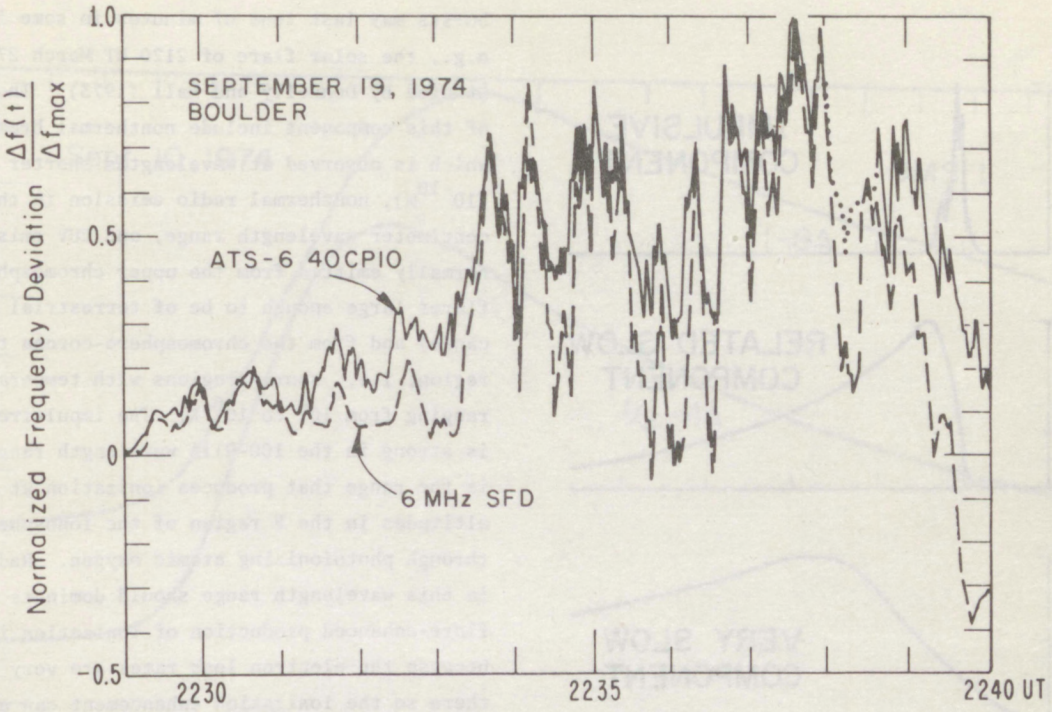

Figure 17. Comparison of ATS-6 and ground-based SFD observations for a flare rich in quasi-periodic fine structure that occurred when the ionosphere and the Earth's magnetic field were disturbed (3 hr Kp = 5-). Δf_{max} = 0.036 Hz on 40 cp 10 and 1.3 Hz on 6 MHz.

discussed qualitatively below that are useful for interpreting the E- and F-region effects of solar flares. From the viewpoint of the terrestrial effects of the ionizing radiations, we are interested mainly in (1) the larger or brighter flares, i.e., large enough to produce detectable terrestrial effects, e.g. Hα importance SB, 1N, 1B, 2N, 2B, and ≥ 3 flares, or 1-8A X-ray flares of class M and X; and in (2) broad wavelength bands, since the terrestrial effects at any height are contributed by a range of X-ray and EUV wavelengths and the terrestrial effects due to any one wavelength occur over a significant range of altitudes. These limitations reduce the variety of flare spectra that need be considered and reduce the importance of the variations in the remaining X-ray and EUV flare spectra. Complexities like emission line broadening and Doppler shifts are negligible for terrestrial applications except for a few lines where the terrestrial absorption cross sections vary greatly with wavelength across the emission line, e.g., C III 977A, where these complexities may achieve minor importance considering the effects of other wavelengths at the same heights involved. Also, the numerous microflares (Wood and Noyes, 1972) with impulsive emissions at wavelengths normally emitted from the chromosphere-corona transition region that lack associated emissions from the upper chromosphere are too small for significant terrestrial effects.

Models for the X-ray and EUV emission have been developed and will be described quantitatively elsewhere (Donnelly, 1976). Qualitatively, these models are based on three time components illustrated in Figure 18. The most important aspect of the model is the definition of the radiation spectra for the three time components. The spectra of these three components are not a simple function of wavelength but rather are ordered according to the solar source-region temperature.

The impulsive component Φ_1 includes a series of fast bursts with rise and decay times of tens of seconds where the series is sometimes quasi-periodic. The ensemble of fast bursts typically rises from start to maximum in several minutes and then decays in a similar time. However, the chain of impulsive

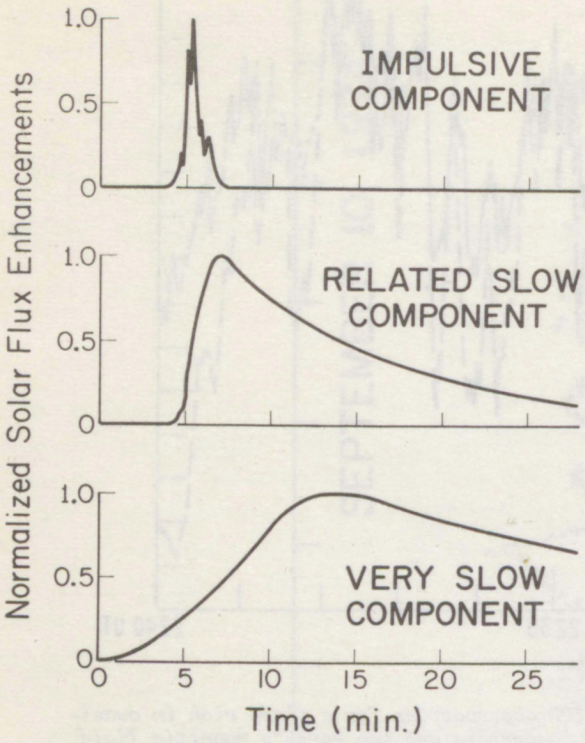

Figure 18. Three time components for models of solar X-ray and EUV flares.

bursts may last tens of minutes in some flares, e.g., the solar flare of 2120 UT March 27, 1967, studied by Donnelly and Hall (1973). The spectra of this component include nonthermal bremmstrahlung, which is observed at wavelengths shorter than 1A (10^{-10}m), nonthermal radio emission in the centimeter wavelength range, and EUV emissions normally emitted from the upper chromosphere (for flares large enough to be of terrestrial significance) and from the chromosphere-corona transition region, i.e., source regions with temperatures ranging from 10^4 to 10^{6}°K. The impulsive component is strong in the 100-911A wavelength range, which is the range that produces ionization at high altitudes in the F region of the ionosphere through photoionizing atomic oxygen. Radiation in this wavelength range should dominate the flare-enhanced production of ionization in SITECs because the electron loss rates are very small there so the ionization enhancement can accumulate. The impulsive flare emission includes emission in the chromospheric H Lyman lines, and the strong ionizing line of C III at 977A. In the 100-911A range important to SITECs, Φ_1 includes the upper chromospheric emissions of the H, He, and He^+ continua and the strong Lyman α line of He II at 304A, and the chromosphere-corona transition emission, e.g., from O IV, O V and including weaker emissions from very high levels of ionization like Mg X, which are partially emitted from source regions with $T_e \lesssim 10^{6}$°K. EUV spectra for the impulsive component of the flare have been reported by Hall and Hinteregger (1969) and Donnelly and Hall (1973). The soft X-ray emission of flares is very weakly influenced by Φ_1; consequently the flare ionizing effects below the bottom of the E layer and in the D region are slow, which is consistent with SFD measurements which show the impulsive component of the time-rate-ofchange of electron density is very weak below the bottom of the E layer.

The "related" slow component Φ_2 is related to the impulsive component in that Φ_2 rises roughly in proportion to the time accumulation of Φ_1, i.e.,

$$\Phi_2(t) \simeq g \int_0^t \Phi_1(u)\, e^{-\frac{t-u}{\tau}}\, du \quad . \qquad [15]$$

Φ_2 starts when Φ_1 starts, rises most rapidly near the peak of Φ_1 and peaks after Φ_1 peaks but before the end of Φ_1. Φ_1 and Φ_2 always occur together. The coefficients g and τ vary with source temperature (or wavelength) and from one flare to another, while τ usually varies slowly during a given flare. The spectrum of Φ_2 is strong for emissions from source temperatures in the range 1-30 x 10^{6}°K, i.e., it is strong in the soft X-ray range (1-100A) and in EUV radiation normally emitted from the corona, e.g., Fe XV 284A and Fe XVI 335A.

The very slow component Φ_3 may occur by itself. When it occurs in conjunction with Φ_1 and Φ_2, the latter usually occur during the rise of Φ_3. The spectrum of Φ_3 is similar to that of Φ_2, i.e., strong in

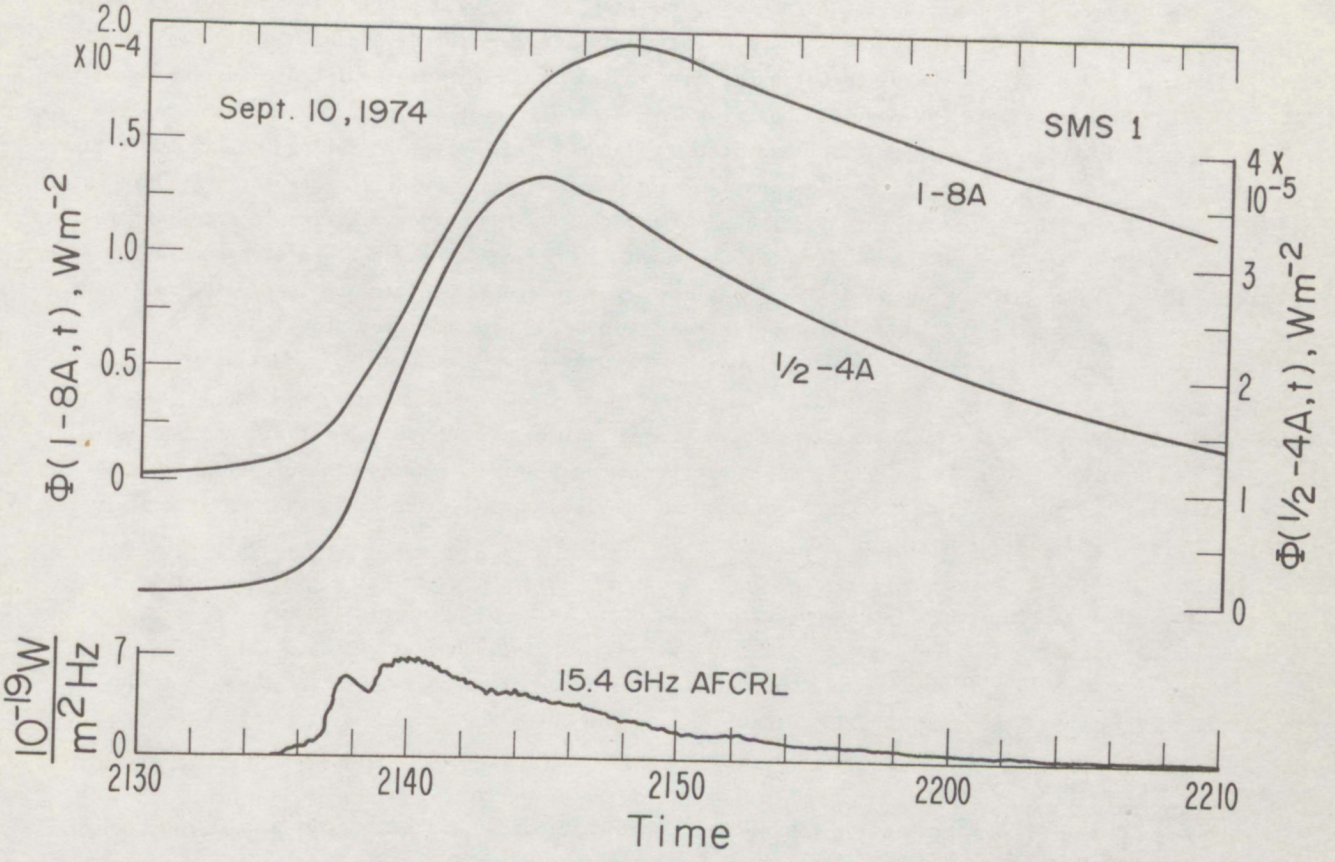

Figure 19. The microwave and soft X-ray bursts for the large flare of September 10, 1974. SMS is the Synchronous Meteorological Satellite.

soft X-rays and coronal emissions, but Φ_2 is relatively stronger for radiations from 5-30 x 10^{6}°K, e.g., in the 1/2 - 3A range. While the emissions at various wavelengths that are affected by Φ_1 have concurrent impulsive time structure, the emissions participating in the slow components have different time dependences ordered according to the solar emission temperature. Emissions from higher temperatures (5 - 30 x 10^{6}°K) peak earlier and decay faster than those from lower coronal temperatures (1 - 5 x 10^{6}°K). The energy flux $\Phi(\lambda_i)$ of any X-ray or emission line at wavelength λ_i, or the energy flux $\Phi(\lambda_i - \lambda_{i+1})$ of a wavelength band of ionospheric interest including continua and minor lines is related to all three components:

$$\phi(\lambda_i,t) = a(\lambda_i)\phi(t) + b(\lambda_i)\Phi_2(\lambda_i,t) + C(\lambda_i)\Phi_3(\lambda_i,t) \text{ Wm}^{-2}. \quad [16]$$

For some flares, Φ_3 is the only component present, but for the flares producing SITECs, Φ_1 and Φ_2 are most important. Soft X-rays are dominated by Φ_2 and Φ_3. The EUV wavelengths dominated by Φ_1 still have some slow emission (Φ_2, Φ_3) resulting from conduction and radiative excitation of the 10^4 to 10^{6}°K solar atmosphere induced by the overlying 1 - 30 x 10^{6}°K coronal flare region.

Figure 19 shows the centimeter wavelength radio burst and soft X-ray fluxes for the flare of September 10, 1974, for which the ATS-6 observations are given in Figures 3, 11, and 16. The X-ray data

indicate the time dependence of the slow emissions. Note that the 1/2-4A X-rays rise faster, peak sooner, and decay faster than the 1-8A X-rays, which is consistent with the 1/2-4A band being more sensitive to 5 - 30 x 10^{6}°K radiation which has a more rapid time structure than that from 1 - 5 x 10^{6}°K. The microwave burst gives a rough indication of the time structure of the impulsive emissions Φ_1 of the flare. We had hoped to use EUV observations from the AE satellite as an indicator of the impulsive EUV flare emissions; however, no AE observations of the solar EUV flux were made during the impulsive flares in Table 3 (D. E. Bedo, AFCRL, private communication). The microwave burst is the best available solar indicator of Φ_1. Since the microwave burst depends directly on the magnetic fields in the flare region whereas the EUV burst does not, and since the GHz burst is more dependent on flare electrons $\gtrsim$ 100 Ke V (Takakura, 1973) whereas the impulsive EUV emissions are more closely related to the 10-100 keV flare electrons (Kane and Donnelly, 1971), the centimeter radio burst does not precisely indicate $\Phi_1(t)$. When the microwave burst has very similar time structure for different frequencies in the 3 - 35 GHz range, then we expect it gives an accurate indication of the impulsive EUV time structure. For all the flares in Table 3, there were significant variations in time structure of the radio burst at frequencies in the 3 - 35 GHz range. For these cases, the highest frequency data having good observations of the impulsive structure were used. The ATS-6 dN_T/dt data provided a good guide as to where the impulsive EUV burst differs from the GHz burst.

The radio burst in Figure 19 is unusual because of the slow decay after 2140 UT. Radio bursts also include slow thermal gradual rise and fall events without impulsive bursts that are related to Φ_3 and similar events with larger superimposed impulsive bursts, i.e., slow post-burst increases that are related to Φ_3 and Φ_2. Some of the slow decay of the radio burst may consist of such thermal radiation but usually the intensity of such radiation is much weaker than that in Figure 19.

Figure 20 and 21 show that using the radio burst to estimate $\Phi_1(t)$ and applying equation (15), the 1 - 8A and 1/2 - 4A soft X-ray emissions can be approximated during their rise and peak using time constants τ of about 15 and 5 min respectively, where τ should be increased during the decay stage ($\tau_{decay} \sim$ 41 and 26 min, respectively). Using different τ's can properly account for the different peak times for Φ(1/2 - 4A) and Φ(1 - 8A). Considering the problems in using the 15 GHz burst in estimating Φ_1 for EUV emission, it is surprising that equation (15) does so well. In a similar manner, all the SITECs in Table 3 fit the case where Φ_1 and Φ_2 dominate the flare radiations where the soft X-ray flux approximately fits Φ_2 in equation [15] with the GHz radio burst used to estimate Φ_1. Φ_3 was needed only for some of the slow events in Table 3 with comment D and for the early small slow rise in soft X-ray emission for some of the other flares. The slow flare on September 22, 1974, probably is a case where the impulsive EUV emission was absorbed in the solar atmosphere since the flare was at the edge of the visible solar disk (west limb) as discussed below.

The flare emissions, particularly the Φ_1 component because of its low-lying source region, depend on the location of the flare on the sun and in the active region, or upon the amount of cool (<10^{6}°K) solar material that lies between the source regions and earth. Soft X-ray flares show no significant dependence on flare location (Drake, 1971) except for flares located beyond the limb of the sun where the soft X-ray bursts tend to have peaks that are flatter with time than the peaks of flares observed on the visible disk (Catalano and Van Allen, 1973). Such beyond-the-limb flares do not produce SITECs because their impulsive 100 - 911A emission is very weak. The impulsive EUV emission decreases for flares near the limb as has been shown through SFDs and is illustrated in Figure 22.

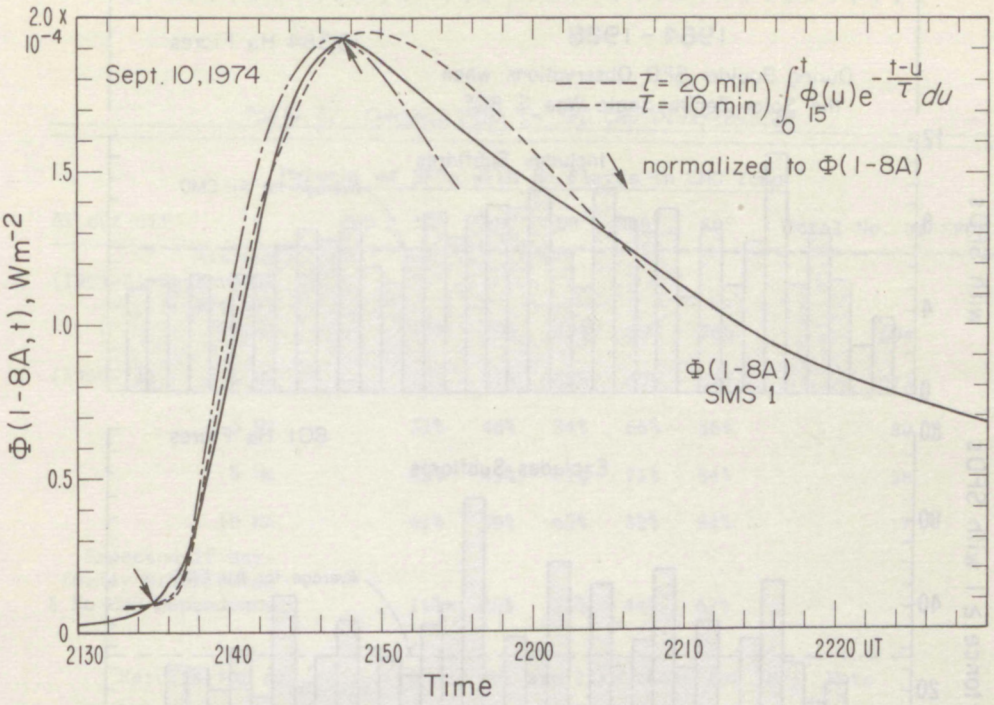

Figure 20. SMS 1 - 8A X-ray flux and normalized Φ_2 time curves based on the 15 GHz radio burst as an estimate of Φ_1. $\tau \approx 15$ min would give a good fit to the main rise and peak while a change to $\tau \approx 41$ min would be needed during the decay phase.

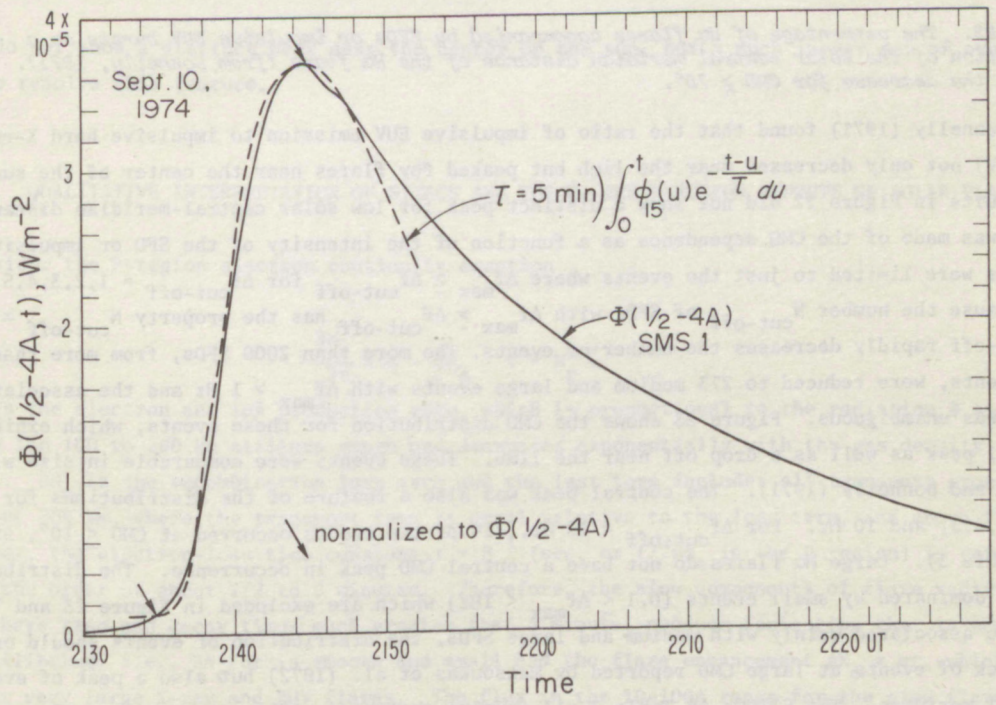

Figure 21. SMS 1/2 - 4A X-ray flux and normalized Φ_2 time curves $\tau \approx 5$ min gives a good fit to the main rise and peak while a change to $\tau \approx 26$ min would be needed to fit the decay phase.

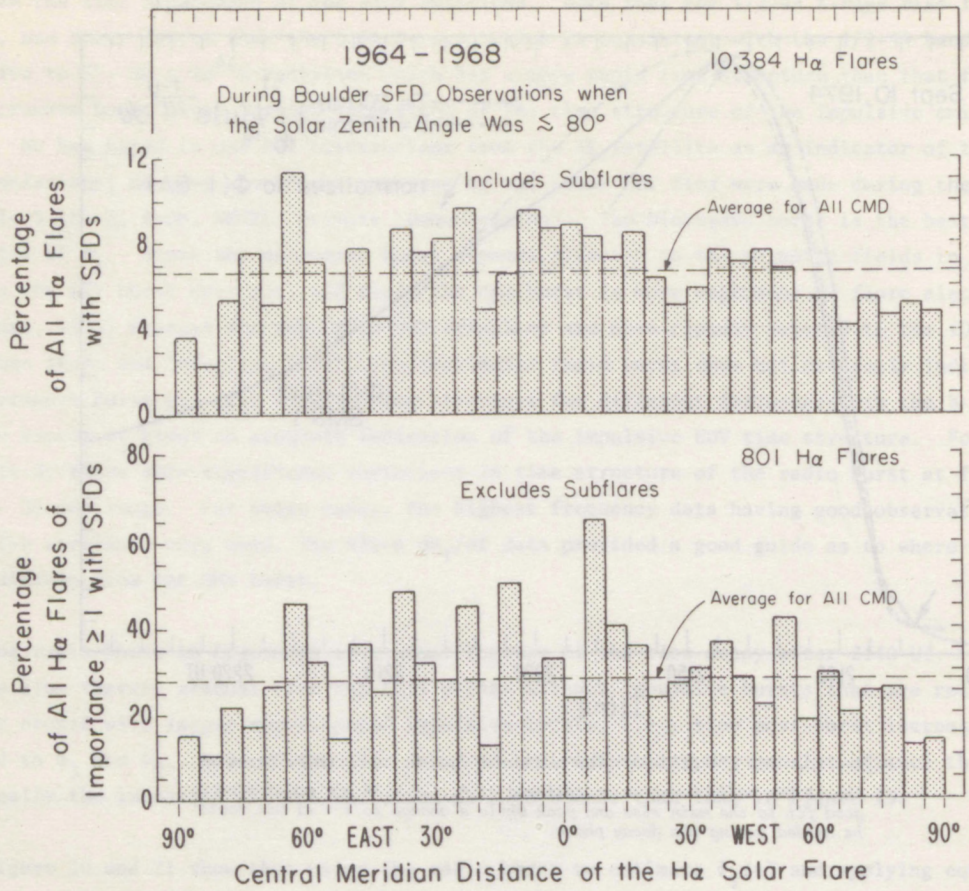

Figure 22. The percentage of Hα flares accompanied by SFDs or impulsive EUV bursts as a function of the solar central meridian distance of the Hα flare (from Donnelly, 1971). Note the decrease for CMD $\gtrsim$ 70°.

Kane and Donnelly (1971) found that the ratio of impulsive EUV emission to impulsive hard X-ray emission (>10keV) not only decreased near the limb but peaked for flares near the center of the sun. Because the results in Figure 22 did not show a distinct peak for low solar central-meridian distances (CMD), a study was made of the CMD dependence as a function of the intensity of the SFD or impulsive EUV burst. The SFDs were limited to just the events where $\Delta f_{max} \geq \Delta f_{cut\text{-}off}$ for $\Delta f_{cut\text{-}off}$ = 1,2,3,4,5, and 10 Hz. Because the number $N_{cut\text{-}off}$ of SFDs with $\Delta f_{max} \geq \Delta f_{cut\text{-}off}$ has the property $N_{cut\text{-}off} \propto 1/\Delta f_{cut\text{-}off}$, raising the cut-off rapidly decreases the number of events. The more than 2000 SFDs, from more than a decade of SFD measurements, were reduced to 273 medium and large events with $\Delta f_{max} \geq 1$ Hz and the associated Hα flare location was unambiguous. Figure 23 shows the CMD distribution for these events, which exhibits a distinct central peak as well as a drop off near the limb. These events were comparable in size with those studied by Kane and Donnelly (1971). The central peak was also a feature of the distributions for $\Delta f_{cut\text{-}off}$ = 2,3,4,5, and 10 Hz. For $\Delta f_{cut\text{-}off}$ = 10 Hz, 41% of the events occurred at CMD $\leq$ 10°, 59% at CMD $\leq$ 20° (Table 5). Large Hα flares do not have a central CMD peak in occurrence. The distribution in Figure 22 is dominated by small events ($0.1 \leq \Delta f_{max} < 1$Hz) which are excluded in Figure 23 and Table 5. Since SITECs are associated mainly with medium and large SFDs, the distribution of events should exhibit not only the lack of events at large CMD reported by Matsoukas et al. (1972) but also a peak of events near the central meridian. The SITECs in Table 3 all involve central meridian distances $\leq$ 62°. Therefore there is a clear lack of SITECs associated with flares near the solar limb which agrees with Matsoukas et al. (1972). On the other hand, the very slow events (comment D) include one flare at the limb and another at W76°; the remainder was an overlapping composite of two flares. The SITECs in

Table 5. Central Peak in SFD CMD Distribution

Δf cut-off		Percent of SFDs with Hα Flares in CMD Zone: CMD ≤ 10°	20°	30°	40°	60°	Total No. of SFDS
(1964-8)	Minimum Observable (i.e., all SFDs)	17%	29%	42%	55%	76%	694
(1960-74)	1 Hz	23%	37%	50%	60%	82%	273
	3 Hz	31%	46%	54%	66%	86%	80
	5 Hz	29%	45%	61%	71%	84%	38
	10 Hz	41%	59%	65%	82%	94%	17
	Expected if Uniformly Distributed & No CMD Dependence	11%	22%	33%	44%	67%	

Results for $\Delta f_{cut\text{-}off} = 2$ and 4Hz are like those for 3Hz. Note how the ratio of observed percent to "No-CMD-Dependence" percent increases as the width of the central CMD zone considered decreases or as $\Delta f_{cut\text{-}off}$ increases. Keep in mind that the latitude of most of these flares is >10° so that the central angle for CMD $\leq$ 10° is still >10°.

Table 3 do not show a distinct peak near the center of the sun, but a much larger set of events is needed to resolve this feature.

8. QUALITATIVE INTERPRETATION OF SITECS AND THE E- AND F-REGION EFFECTS OF SOLAR FLARES

Consider the F-region electron continuity equation

$$\frac{\partial N_e}{\partial t} = q - \beta N_e - \nabla \cdot N_e \vec{v} \qquad [16]$$

where q is the electron and ion production rate, which is proportional to the radiation Φ and is large mainly in the 100 to 200 km altitude range and decreases exponentially with the gas density at higher altitudes. βN_e is the recombination loss term and the last term includes all transport processes. Below about 200 km, where the transport term is small relative to the loss term, and above the bottom of the E layer, the electron-loss time constant $\tau = \beta^{-1}$ (sec, or $1/2\alpha N_e$ in the E region) is very small, i.e., of the order of about 1/2 to 2 minutes. Therefore, the slow components of flare radiation, Φ_2 and Φ_3 which have rise and decay times much greater than a minute, produce ionization that is nearly in quasi-equilibrium, i.e., $\partial N_e/\partial t$ is smooth and small and the flare enhancement $\Delta N_e \simeq q\tau$, which is small except for very large X-ray and EUV flares. The flux in the 10-100A range for the slow flare components is very strong in absolute flux and slower than the 1 - 10A flux. Because of the K-shell absorption edge of N_2 at about 30A, the 10 - 30A photoionization occurs at the same heights as that from 30 - 100A radiation. This fold-over in the production height curves results in a large and long lasting enhancement

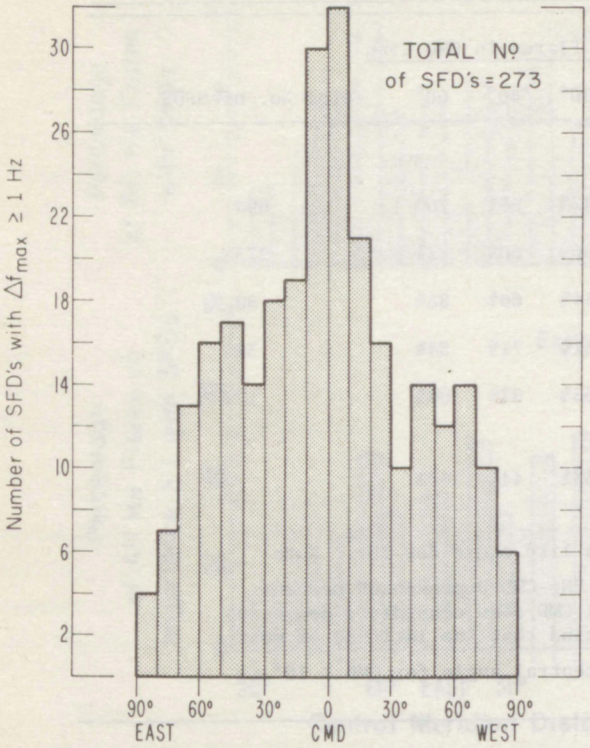

Figure 23. Distribution by solar central-meridian distance of Hα flares accompanied by SFDs of $\Delta f_{max} \geq 1$ Hz.

of ionization in the 100 to 140 km altitude range, like those observed by Thome and Wagner (1971). The EUV emission Φ_1 in the 911-1030A, e.g., C III 977A and H Ly β 1026 A, produce impulsive ionization enhancements in this altitude range early in flares, which will be discussed below, but do not contribute much to the long lasting ionization enhancement. The 1 - 10A slow X-ray bursts have extremely large percentage enhancements and produce large percentage ionization enhancements in the 80 - 100 km altitude range. Despite the large photoionization rates below 200 km, the net production of ionization is inefficient for the slow components Φ_2 and Φ_3, i.e., $\Delta N_e \propto \tau \Phi_{2+3}$.

Above 200 km the βN_e loss term drops to small values because of the low molecular neutral densities, which result in low loss rates for the dominant ion O^+ (H^+ and He^+ at very high altitudes). Although the photoionization rate q is small and decreases exponentially with altitude, the efficiency of net ionization production is greatly increased because τ at high enough altitudes is large with respect to the rise and decay time constants of the impulsive component Φ_1, the slow component Φ_2, and at very high altitudes, Φ_3. Then roughly $\Delta N_e \propto \int_0^t \Phi_{1+2+3} dt$, i.e., the ionization accumulates. This contributes to the large, slow ionization enhancements observed by Thome and Wagner (1971) above 200 km. The small slow enhancement of dN_T/dt ($\propto \Delta f$) during the flare of September 10 from 2131 to 2135 UT (see Figure 16) and from 2143 to 2153 UT results in a significant contribution to ΔN_{T2max}. This contribution occurs at altitudes above 200 km as evidenced by concurrent ground-based SFD data where these slow features are absent.

Considering Mendillo and Evan's (1974) incoherent scatter observations of the largest SITEC observed, the transport term is clearly important in influencing the height distribution of the flare-induced ionization and therefore the rate of loss of electrons above 200 km. Although the transport term is small relative to recombination loss rates below 200 km, the net flare-enhanced upward flux of photo-electrons and thermal electrons at 200 km may be an important source of ionization above 200 km, where the loss rates are low. The influence of transport will be studied through detailed ionospheric-model computer calculations. The main qualitative point we can make is that high altitude photoionization is an important source of the ionization enhancement above 200 km that dominates ΔN_{T2max} of SITECs. Consider the case where $\int_{200km}^{\infty} \Delta q \, dh \simeq 0.1 \Delta Q_T$, as estimated for the August 28, 1966 flare at 1527 UT (Donnelly, 1968), where $Q_T = \int_0^{\infty} q \, dh$ and the Δ's refer to the flare enhancements. Then roughly $\int_{200}^{\infty} \Delta N_e \, dh \simeq 0.1 \bar{\eta} \int_0^t \Delta Q_T dt$

for t small relative to the loss time constants where $\bar{\eta}$ is an effective ionization efficiency. Also $\int_0^{200\ km} \Delta N_e\ dh \approx \tau\bar{\eta}\Delta Q_T$ where τ below 200 km averages about 1/2 minute. For a radiation burst with a rise time of about 10 minutes, then $\int_{200}^{\infty} \Delta N_e\ dh \sim 1/2\ \Delta N_T$. Therefore, the relatively weak photoionization at high altitudes (>200 km) can be a significant source of the high altitude ionization enhancement that dominates ΔN_{Tmax} of SITECs.

The photoionization above 170 km for most ionizing radiations is in the optically thin region and is weakly dependent on the solar zenith angle except for very large zenith angles (χ>80°). Therefore the ionization enhancements at high altitudes that dominate SITECs (ΔN_{T2max}) should be relatively independent of the solar zenith angle, as was observed in the August 7, 1972, SITEC (Mendillo et al., 1974). The occurrence of events in Table 3 shows no simple relation to solar zenith angles during the daylight hours at Boulder. Furthermore, the high altitude photoionization is much more sensitive to 100-911A radiation than to either the soft X-rays <100A or ultraviolet >911A, because of the large atomic oxygen photoionization cross sections in the 100-911A range; consequently, the large percentage flux increases of Φ_2 or Φ_3 in the 1-100A range have less effect on SITECs than their 100-911A flux increase which is comparable in absolute flux.

Consider now the impulsive EUV emissions Φ_1 that are weak in the 1-50A range but strong in the ionizing 50-1026A range, particularly in the 100-911A range, which is important for high altitude photoionization. The rise and decay times of about 10 sec for individual component bursts of Φ_1 are smaller than the E- and F1-region electron-loss time constants and much smaller than the F2-region loss time constants. On the other hand, the ensemble of Φ_1 bursts tend to have start-to-peak or peak-to-end times ranging from being comparable with, up to being much larger than E- and F1-region loss time constants. See Figure 19, where the GHz radio burst gives a rough estimate of $\Phi_1(t)$. Consequently, according to (16), $\partial N_e/\partial t$ in the E and F1 region tends to mimic the individual impulsive bursts or rapid rises in Φ_1. However, the loss term significantly affects $\partial N_e/\partial t$ during the peak and decay of the ensemble of impulsive bursts. Much of the large impulsive peaks of the ATS-6 dN_T/dt comes from the 100 - 200 km altitude region of large photoionization since this high-loss region is far from equilibrium for such impulsive radiation bursts. The SFD Δf curve in Figure 16, which is proportional to $\partial N_e/\partial t$ in the E and F1 region, peaks during the rapid rises of the 15-GHz burst but is mainly negative during the main peak and decay of the 15-GHz burst. This is consistent with the time constants of the radiation burst and the E- and F1-region loss rates. These high loss rates and the impulsiveness of the 100-911A radiation cause the flare-induced ionization enhancement in the 140 - 200 km altitude range to decay rapidly relative to the effects above 200 km (low-loss region) or below 140 km (slow photoionization region), as was observed by Thome and Wagner (1971). On the other hand, the ATS-6 dN_T/dt observations of the event on September 10 remained mostly positive from 2140 to 2153 UT, i.e., the positive $\partial N_e/\partial t$ results above 200 km were greater than the negative values below 200 km because of the low-loss rates at high altitudes. The impulsive increases from Φ_1 dominated the net ΔN_T, e.g., as evident in Figures 11 and 16. The loss of ionization in the 140 - 200 km altitude range during the decay of Φ_1 is compensated for in the SITEC data by the continued accumulation at high altitudes of ionization from Φ_1 and by the rise and peak of Φ_2. The lack of SITECs for flares with large CMD results from Φ_1 or the 100-911A flare emission being relatively weak for flares near or beyond the limbs of the sun as shown in Figures 22 and 23.

Three types of flare-related events in total content have been identified including two types of SITECs, one that decayed rapidly after the end of its rapid rise and another that slowly continued to a flat maximum. Furthermore, two maxima in ΔN_T were considered, one ΔN_{T1max} shortly after the rapid rise

in ΔN_T where in some events this feature was a point of inflection in $\Delta N_T(t)$ rather than a true maximum, and a second later one, ΔN_{T2max}, which for most events was a slow flat maximum but for the fast-decay type of SITEC did not occur. The fast-decay SITECs occurred during ionospheric storms, when the upper atmosphere is richer in molecular constituents (Prölss and von Zahn, 1974; Reber et al., 1973) which cause high electron loss rates, and during radiation bursts that decayed fairly rapidly. Some SITECs during disturbed periods where the soft X-rays were long lasting did not decay rapidly, e.g., the SITEC of 1510 UT July 5, 1974, in Figure 9, where apparently the long lasting flare radiation prolonged the SITEC. SITECs where the soft X-ray flux decayed rapidly yet the Earth's magnetic field was relatively quiet (1743 UT October 8 and 1732 UT October 11, 1974) exhibited only a small initial rapid decay followed by a larger very slow decay. Hence, extensive rapid decay of SITECs requires both rapid decay of the flare radiation and ionospheric storm conditions. Our interpretation of these fast events is that the F-region electron loss rates were higher than usual so that the high-altitude accumulation of ionization fell sharply with the rapid decline of radiation which resulted in one maximum ΔN_{T1} shortly after the peak in the 100-911A radiation, Φ_1, followed by a loss-dominated decay of ΔN_T (see, e.g., Figure 10).

The sustained SITECs occur when the flare radiation is long lasting or during geomagnetically quiet periods. Those occurring during quiet periods, e.g., the September 10 flare in Figure 11, tended to have the time $t_{\Delta Nmax1}$ occur later with respect to t_I, the time of the peak of Φ_1 as indicated by the maximum of the radio burst in Table 3, than did the events during magnetically active periods [$(\overline{t_{\Delta Nmax1} - t_I}) \simeq 3$ min. for $\bar{K}_p \leq 3$, 1/2 min. for $\bar{K}_p \geq 3$]. The slow second type of ΔN_T maximum usually occurred after the slow 1-8A soft X-ray maximum (t_s); however, the unobserved soft X-rays at $\lambda > 8$A would also peak later than 1-8A. Therefore it is not clear for most events how much of the delay in peak times ($t_{\Delta Nmax2} - t_s$) is due to the continued accumulation of ionization above 200 km during the slow decay of flare radiation until the loss rates finally balance the production rate ($dN_T/dt = 0$). The SITEC on September 10 in Figure 11, when the Earth's magnetic field was very quiet, appears to have accumulated ionization during the slow decline in soft X-rays (Figure 19) because the soft X-rays at $\lambda > 8$A probably peaked before 2150 UT based on the 1/2 - 4A and 1 - 8A data and empirical trends in soft X-ray peak times.

9. CONCLUSIONS

The ATS Boulder observations of events in total electron content related to X-ray and EUV bursts of solar flares given in Tables 3 and 4 exceed past observations in both time and electron content resolution. The high resolution ATS-6 data permitted study of the time-rate-of-change of total electron content (dN_T/dt) and for the first time permitted direct quantitative comparison with concurrent SFD observations. These comparisons showed that dN_T/dt during SITECs is dominated by the large impulsive structure observed by SFDs and caused by impulsive EUV burst. The ATS-6 dN_T/dt data were found to be essentially transionospheric SFD measurements. However dN_T/dt also includes a small long-lasting component produced in the F_2 region by the slow flare radiations. The comparison with SFD data shows that by the time the slow maximum enhancement ΔN_{Tmax} in total electron content is reached, most of the flare ionization in the upper E and F_1 regions, where electron loss rates are high, has decayed significantly. Therefore most of ΔN_{Tmax} comes from the accumulation of ionization in the low-loss F_2 region above 200 km, in agreement with incoherent scatter measurements. The impulsive 100-911A EUV emissions dominate this high altitude increase in ionization but the slow X-ray and EUV flare enhancements are a significant secondary source particularly during the slow maximum (ΔN_{Tmax2}) and decay phase.

Three types of event in total electron content related to solar flares were identified; two of these qualify as SITECs. The first and main type of SITEC involves a rapid rise in total electron content followed by a slow flat maximum and slow decay. These events occur either when ionospheric storms are not in progress or when the flare radiation is long lasting. The second type of SITEC decays rapidly after the impulsive EUV burst and occurs when both the flare radiation decays relatively rapidly and an ionospheric storm is in progress causing anomalously high electron loss rates in the F_2 region. The impulsive 100-911A burst produces the main contribution to both types of SITECs.

The third type of total electron content event related to solar flares is slow rather than sudden. These events are very indistinct because they lack the distinctive rapid features of SITECs and they look like the effects from other ionospheric variations. They are evident from comparing data from different ground stations (spatial diversity), because the flare effects occur over the whole sunlit hemisphere, and from close comparison with satellite soft X-ray data. The flares involved are weak in impulsive 100-911A flux either because the flare was located near the solar limb or behind cool structures of a solar active region where strong absorption of the impulsive EUV burst occurs, or the flare was a thermal gradual-rise-and-fall type. Soft X-ray flares comparable in magnitude with soft X-ray flares listed in Table 3, and therefore having comparable D- and E-region slow effects, definitely occur with no distinct F-region effects because the flares are too weak in 100-911A emission, e.g., beyond-the-limb flares, near-limb flares, and thermal gradual-rise-and-fall events.

SITECs, like SFDs, were found to be preferentially produced by flares located on the solar disk and away from the solar limbs, in agreement with Matsoukas et al. (1972). This preference results from SITECs being strongly dependent on the impulsive 100-911A bursts and impulsive EUV bursts decrease in intensity with increasing solar central-meridian distance (CMD). (Soft X-ray bursts, and hence D-region SIDs, do not exhibit a dependence on CMD $\leq 90°$ and even include beyond-the-limb flares.) SITECs during the morning rapid rise in total content were more difficult to distinguish, i.e., high resolution data were required, but a shortage of SITECs during the morning hours was not found.

10. ACKNOWLEDGMENTS

We thank our colleagues: J. D. Hargreaves, R. N. Grubb, and K. Davies for planning and developing the excellent ATS-6 radio beacon; R. N. Grubb, J. E. Jones, and J. H. Taylor for developing the excellent receiving and recording systems at Boulder; C. L. Rufenach for providing the final motivation for including the high resolution ϕ_{40CP10} channel, which provided our best data on the solar flare effects in the F region; J. Falcon, L. Matheson, and C. Candelaria for processing the ATS-6 data; G. Paul and L. R. Wescott for processing ionograms; E. L. Berger and G. M. Lerfald for the Boulder SFD data; K. Najita for the University of Hawaii SFD data and B. Henson for SFD data from Huntsville, Alabama; and K. C. Yeh of the University of Illinois and J. A. Klobuchar of AFCRL for sending copies of their SITEC data. We appreciate the solar microwave data provided by A. Covington, NRC, Ottawa; by J. Castelli, AFCRL; by D. S. Lund, NOAA; and by Manila Observatory. We're also thankful to F. C. Cowley and P. Hill for processing the SMS-1 soft X-ray data. We gratefully acknowledge the financial support of NASA Order Numbers S-70200 A and W13,938, without which our analysis of the SITEC observations would not have been possible.

REFERENCES

Bennett, J. A. (1967) The calculation of Doppler shifts due to a changing ionosphere, *J. Atmosph. Terr. Phys.*, 29, 887-91.

Cain, J. C. and R. E. Sweeney (1970), Magnetic field mapping of the inner magnetosphere, *J. Geophys. Res.* 75, 4360-2.

Catalano, C. P. and J. A. Van Allen (1973), Height distribution and directionality of 2-12A X-ray flare emission in the solar atmosphere, *Astrophys. J.* 185, 335-49.

Davies, K., R. B. Fritz, R. N. Grubb and J. E. Jones (1975), Some early results from the ATS-6 radio beacon experiment, *Radio Science*, 10, 785-99.

Davies, K., R. B. Fritz and T. B. Gray (1976) Measurements of the columnar electron contents of the ionosphere and plasmasphere, submitted for publication in *J. Geophys. Res.*

Donnelly, R. F. (1968). An Analysis of Sudden Ionospheric Disturbances Associated with the Proton Flare of 1522 UT, August 28, 1966, ESSA Tech. Rept. ERL 92-SDL6. (U. S. Government Printing Office).

Donnelly, R. F. (1971), Extreme ultraviolet flashes of solar flares observed via sudden frequency deviations: experimental results. *Solar Phys.* 20, 188-203.

Donnelly, R. F. (1973), Ground-based observations of EUV flare emissions, High Energy Phenomena on the Sun, eds. R. Ramaty and R. G. Stone, NASA SP-342, 242-61 (U. S. Government Printing Office, Washington, D. C. 20402).

Donnelly, R. F. (1976), Empirical models of solar flare X-ray and EUV emission for use in studying the E- and F-region effects of solar flares, to be submitted to *J. Geophys. Res.*

Donnelly, R. F. and L. A. Hall (1973) Extreme ultraviolet spectrum of the solar flare of 2114 UT March 27, 1967, *Solar Phys.*, 31, 411-26.

Donnelly, R. F., A. T. Wood, Jr. and R. W. Noyes (1973), The extreme ultraviolet emissions of solar flares: a comparison between OSO-6 spectroheliograph observations and SFDs, *Solar Phys.*, 29, 107-123.

Donnelly, R. F., E. L. Berger, Lt. J. D. Busman, B. Henson, T. B. Jones, G. M. Lerfald, K. Najita, W. M. Retallack and W. J. Wagner (1974). An Atlas of Extreme Ultraviolet Flashes of Solar Flares Observed via Sudden Frequency Deviations During the ATM-Skylab Missions, Report UAG-36, World Data Center A for Solar-Terrestrial Physics, U. S. Department of Commerce, National Oceanic and Atmospheric Administration, Environmental Data Service, Asheville, North Carolina, U.S.A., 28801.

Drake, J. F. (1971) Characteristics of soft solar X-ray bursts, *Solar Phys.* 16, 152-85.

Garriott, O. K., A. V. da Rosa, M. J. Davis and O. G. Villard, Jr., (1967), Solar flare effects in the ionosphere, *J. Geophys. Res.* 72, 6099-103.

Garriott, O. K., A. V. da Rosa, W. J. Ross (1970), Electron content obtained from Faraday rotation and phase path length variations, *J. Atmosph. Terr. Phys.* 32, 705-27.

Hall, L. A. and H. E. Hinteregger (1969), Solar EUV enhancements associated with flares, in Solar Flares and Space Research, COSPAR Symp., C. de Jager and Z. Svestka, eds., North-Holland, Amsterdam, 31-36.

Hargreaves, J. K. (1970), ATS-F: observational opportunities, in Proc. Symp. Future Application of Satellite Beacon Experiments, Max-Planck Institut fur Aeronomie, Lindau/Harz, West Germany, 16-1 to 16-9.

Jones, R. M. (1966) A three-dimensional ray tracing computer program, ESSA Tech. Report IER17-ITSA 17 (U. S. Government Printing Office, Washington, D. C. 20402).

Jones, R. M. and J. J. Stephenson (1975) A versatile three-dimensional ray tracing computer program for radio waves in the ionosphere, Tech. Report OT TR75-6 (U. S. Government Printing Office, Washington, D. C. 20402).

Kane, S. R. and R. F. Donnelly (1971) Impulsive hard X-ray and ultraviolet emission during solar flares, *Astrophys. J.* 164, 151-163.

Matsoukas, C. A., M. D. Papagiannis, J. Aarons and J. A. Klobuchar (1972), Correlation of solar radio bursts and sudden increases of the total electron content (SITEC) of the ionosphere, *J. Atmosph. Terr. Phys.* 34, 1275-83.

Mendillo, M. and J. V. Evans (1974) Incoherent scatter observations of the ionospheric response to a large solar flare, *Radio Sci.*, 9, 197-203.

Mendillo, M., J. A. Klobuchar, R. B. Fritz, A. V. da Rosa, L. Kersley, K. C. Yeh, B. J. Flaherty, S. Rangaswamy, P. E. Schmid,. J. V. Evans, J. P. Schödel, D. A. Matsoukas, J. R. Koster, A. R. Webster, and P. Chin (1974), Behavior of the ionospheric F region during the great solar flare of 7 August 1972, *J. Geophys. Res.* 79, 665-72.

Mitra, A. P. (1974), Ionospheric Effects of Solar Flares, D. Reidel Publ. Co., Dordrecht, Holland.

Papagiannis, M. D. and D. A. Matsoukas (1971), Simultaneous sudden frequency deviations and sudden enhancements of the total electron content of the ionosphere, *Nature Phys. Sci.*, 233, 55-6.

Prölss, G. W., and U. von Zahn (1974), ESRO 4 gas analyzer results: 2 direct measurements of changes in the neutral composition during an ionospheric storm, *J. Geophys. Res.*, 79, 2535-9.

Reber, C. A., A. E. Hedin and S. Chandra (1973), Equatorial phenomena in neutral thermospheric composition, *J. Atmosph. Terr. Phys.*, 35, 1223-8.

Takakura, T. (1973), Theory of Microwave and X-Ray Emission, in High Energy Phenomena on the Sun, eds. R. Ramaty and R. G. Stone, (U. S. Government Printing Office, Washington, D. C., 20402), 179-187.

Taylor, G. N. (1975) Incoherent scatter measurements of E- and upper D-region ionization changes during three solar flares, *J. Atmosph. Terr. Phys.* 37, 349-57.

Thome, G. D. and L. S. Wagner (1971) Electron density enhancements in the E and F regions of the ionosphere during solar flares, *J. Geophys. Res.* 76, 6883-95.

Wood, A. T., Jr. and R. W. Noyes (1972) Solar flares in the extreme ultraviolet II. Comparisons with other observations, *Solar Phys.* 24, 180-96.

☆U.S. GOVERNMENT PRINTING OFFICE: 1975 — 677-347 / 1227 REGION NO. 8

ENVIRONMENTAL RESEARCH LABORATORIES

The mission of the Environmental Reasearch Laboratories is to study the oceans, inland waters, the lower and upper atmosphere, the space environment, and the earth, in search of the understanding needed to provide more useful services in improving man's prospects for survival as influenced by the physical environment. Laboratories contributing to these studies are:

Atlantic Oceanographic and Meteorological Laboratories (AOML): Geology and geophysics of ocean basins and borders, oceanic processes, sea-air interactions and remote sensing of ocean processes and characteristics (Miami, Florida).

Pacific Marine Environmental Laboratory (PMEL): Environmental processes with emphasis on monitoring and predicting the effects of man's activities on estuarine, coastal, and near-shore marine processes (Seattle, Washington).

Great Lakes Environmental Research Laboratory (GLERL): Physical, chemical, and biological, limnology, lake-air interactions, lake hydrology, lake level forecasting, and lake ice studies (Ann Arbor, Michigan).

Atmospheric Physics and Chemistry Laboratory (APCL): Processes of cloud and preciptation physics; chemical composition and nucleating substances in the lower atmosphere; and laboratory and field experiments toward developing feasible methods of weather modification.

Air Resources Laboratories (ARL): Diffusion, transport, and dissipation of atmospheric contaminants; development of methods for prediction and control of atmospheric pollution; geophysical monitoring for climatic change (Silver Spring, Maryland).

Geophysical Fluid Dynamics Laboratory (GFDL): Dynamics and physics of geophysical fluid systems; development of a theoretical basis, through mathematical modeling and computer simulation, for the behavior and properties of the atmosphere and the oceans (Princeton, New Jersey).

National Severe Storms Laboratory (NSSL): Tornadoes, squall lines, thunderstorms, and other severe local convective phenomena directed toward improved methods of prediction and detection (Norman, Oklahoma).

Space Environment Laboratory (SEL): Solar-terrestrial physics, service and technique development in the areas of environmental monitoring and forecasting.

Aeronomy Laboratory (AL): Theoretical, laboratory, rocket, and satellite studies of the physical and chemical processes controlling the ionosphere and exosphere of the earth and other planets, and of the dynamics of their interactions with high-altitude meteorology.

Wave Propagation Laboratory (WPL): Development of new methods for remote sensing of the geophysical environment with special emphasis on optical, microwave and acoustic sensing systems.

Marine EcoSystem Analysis Program Office (MESA): Plans and directs interdisciplinary analyses of the physical, chemical, geological, and biological characteristics of selected coastal regions to assess the potential effects of ocean dumping, municipal and industrial waste discharges, oil pollution, or other activity which may have environmental impact.

Weather Modification Program Office (WMPO): Plans and directs ERL weather modification research activities in precipitation enhancement and severe storms mitigation and operates ERL's research aircraft.

NATIONAL OCEANIC AND ATMOSPHERIC ADMINISTRATION
BOULDER, COLORADO 80302